Single-Layer Surface Quasicrystals of Identical Particles in Hyperspace

Master's Thesis in Physics

Presented by

Johannes Schöttner

March 16, 2023

Institut für Theoretische Physik I
Friedrich-Alexander-Universität Erlangen-Nürnberg

Supervisor: Prof. Dr. Michael Schmiedeberg

Eidesstattliche Erklärung

Hiermit erkläre ich, dass ich die vorliegende Arbeit selbstständig angefertigt, nicht anderweitig zu Prüfungszwecken vorgelegt und keine anderen als die angegebenen Hilfsmittel verwendet habe. Sämtliche wissentlich verwendete Textausschnitte, Zitate oder Inhalte anderer Verfasser wurden ausdrücklich als solche gekennzeichnet.

Datum	Unterschrift

Abstract

The concept of hyperspace can be used, among other things, to describe non-periodic structures and their degrees of freedom. A phasonic **M**onte **C**arlo (MC) simulation is used to study surface quasicrystals. Additionally, neural networks were trained to perform regression analysis of hyperangles and phasonic flips.

Zusammenfassung

Das Konzept des Hyperraums kann unter anderem genutzt werden, um nicht-periodische Strukturen und ihre Freiheitsgrade zu beschreiben. Eine phasonische **M**onte **C**arlo (MC) Simulation wird verwendet, um Oberflächenquasikristalle zu untersuchen. Darüber hinaus werden neuronale Netze trainiert, um Regressionsanalysen von Hyperwinkeln und phasonischen Flips durchzuführen.

Acknowledgement

I would like to sincerely thank Prof. Michael Schmiedeberg for his guidance and excellent supervision throughout my master's thesis.

Contents

1 Introduction

Quasicrystals are structures without translational symmetry. They often are described as projections of higher-dimensional structures. While symmetries occurring in periodic crystals are given by the crystallographic point groups, quasicrystals are characterized by the existence of unusual point groups and phasonic degrees of freedom. Quasicrystals can grow in a self-assembled manner. The stability of quasicrystals partially is due to the fact that they can have more degrees of freedom and therefore higher entropy than periodic crystals. In fact, most known quasicrystals are high-temperature phases[1].

Literature research on axial quasicrystals of identical particles

Colloids are approximately identical micron-sized particles dispersed in a solvent. Because of their size, colloids are easier to handle and to observe than atoms, while undergoing Brownian motion. By preventing aggregation they can be used as a mesoscopic model for quasicrystals. Quasicrystals can form by applying a suitable external field. They can also self-assemble using modified interaction potentials with quasicrystalline length scales or with preferred binding angles. Colloids provide insight into fundamental quasicrystalline principles, like emergence of special tilings, stability of a desired rotational symmetry, occurrence of phasonic excitation; suitable parameters for self-assembly in experiments can be proposed[2, 3].

In 2013 Stefan Förster *et al.* discovered a new class of materials: **oxide** quasicrystals with a nano length scale. They arise from a multilayer heteroepitaxy of a perovskite on the substrate $Pt(111)$. Monoatomic layers of ternary oxides are formed. For example, a Niizeki-Gähler tiling and a 12-fold rotational symmetry can be identified. Depending on the heating temperature of the annealing process, different long-range orders can develop[4, 5].

Motivation

In section 2 and 3, it is explained that many quasicrystals, as well as their degrees of freedom, can be described by using a higher-dimensional periodic crystal. A quasicrystal occupies certain lattice points of the hyperspace. *Phasonic flips* correspond to jumps to certain neighboring unoccupied lattice sites. They are proposed in the MC simulation to relax the quasicrystal in its phasonic degrees of freedom. Phasonic flips are largely correlated with one another. The simulation corresponds to a locally non-isomorphic mapping into the *random tiling regime*, which includes tilings that can be reached by single phasonic flips and are mostly energetically close to the ideal tiling, for an interaction potential that stabilizes the occurring length scales.

In section 4 the phasonic dynamics of an 8-fold axial quasicrystal on a substrate is simulated in hyperspace. The phasonic distortion and emerging anisotropies are investigated. With this simulation method, the hyperspace coordinates of the particles are known at all times. Material properties can be better understood with an overview of the distribution of phasonic flips. With knowledge of the phasonic distortion, quasicrystals can be produced in the laboratory. Michael Schmiedeberg *et al.* showed that a substrate potential with phononic and phasonic distortions can be generated by slightly misaligned laser beams[6].

Quasicrystals can be observed or simulated directly in physical space, but to investigate them, a reconstruction in hyperspace is extremely helpful. Johannes Hielscher *et al.* reconstructed quasicrystals in a suitable hyperspace by approximately assigning particles to hyperlattice sites[7]. A good knowledge of the quasicrystal simplifies this task. For this purpose, in section 5 neural networks are trained to recognize hyperangles and to localize phasonic defects.

2 Hyperlattice description of quasicrystals

In the following, the cut-and-project method is presented for the construction of quasicrystals and periodic approximants in a hyperlattice. For surface crystals, *axial* quasicrystals are particularly suitable. These are two-dimensional quasicrystals that can form three-dimensional layers. Other quasicrystals are *icosahedral*; these are aperiodic in any direction. With this method the one-dimensional Pell quasicrystal and a possible approximant are generated. An Ammann-Beenker tiling is also demonstrated as an example for a two-dimensional generalization.

The term hyperlattice is used for a *point lattice* of dimension n; here we use a discrete orbit of a Z-module in the euclidean space E^n. It is therefore generated by n independent vectors corresponding to a representation of the general linear group $\mathrm{GL}(n, \mathbb{Z})$ and it is isomorphic to $\mathbb{Z}^n$. The prerequisite for the cut-and-project method is an invertible mapping. In the following, mostly elements of the symmetry group are used, for example, to construct the Ammann-Beenker tiling.

2.1 Crystallographic restriction

The *crystallographic restriction* Ord_n defines the dimension of the hyperlattice n in which a particular order of a mapping occurs. It is defined according to [8, 9] by:

$$\mathrm{Ord}_n = \{m \in \mathbb{N} \mid \exists A \in \mathrm{GL}(n, \mathbb{Z}) \text{ with } \mathrm{Ord}(A) = m\}$$

Where A is an integer matrix. The order of A is the smallest $k \in N^+$ for $A^k = I$; else of infinite order. The minimal embedding is given by the Euler totient function $\varphi(m)$:

$$\varphi(m) = m \prod_{p|m} \left(1 - \frac{1}{p}\right)$$

For $m > 2$ and p only prime numbers. $\varphi(m)$ is even: the smallest dimension where symmetries can be observed is even. A group compatible with a lattice can be represented as integer matrices, by choosing the corresponding basis. For the cut-and-project method often the isometry group is considered. An *isometry* is a map that preserve the metric. A linear isometry keeps the origin fixed.

2.2 Symmetry group of order 4

A hyperspace dimension of $n \geq 4$ is required in order to construct a two-dimensional quasicrystal with a quasicrystalline rotational symmetry. This can be seen by calculating the crystallographic restriction:

- $\mathrm{Ord}_2 = \mathrm{Ord}_3 = \{1, 2, 3, 4, 6\}$
- $\mathrm{Ord}_4 / \mathrm{Ord}_2 = \{5, 8, 10, 12\}$

In the following, the cubic lattice $\mathbb{Z}^4$ is used to create two-dimensional quasicrystalline structures. Therefore the point group O(2) will be considered; for this linear isometry a symmetry-adapted basis will be chosen. Every linear isometry can be represented for a certain orthonormal basis by a $n \times n$ block diagonal matrix R, where each block R_i is either fixed ± 1 or stabilized:

$$R_i = \begin{bmatrix} \cos\Theta_i & -\sin\Theta_i \\ \sin\Theta_i & \cos\Theta_i \end{bmatrix}$$

In the case of the 4-dimensional Euclidean space E^4 it's given by:

$$R = \begin{bmatrix} \cos\alpha & -\sin\alpha & 0 & 0 \\ \sin\alpha & \cos\alpha & 0 & 0 \\ 0 & 0 & \cos\beta & -\sin\beta \\ 0 & 0 & \sin\beta & \cos\beta \end{bmatrix}$$

If you choose $\alpha = \frac{2\pi}{k_\alpha}$ and $\beta = \frac{2\pi}{k_\beta}$ with $k_i \in \mathbb{N}$, the order of the combined cyclic group is given by $k_\alpha \cdot k_\beta$. By choosing a basis, the hyperspace E^4 can be separated into two-dimensional subspaces[10]:

$$E^4 = E^{\|} \oplus E^{\perp}$$

2.3 Acceptance window

The orbits of the Z-modules are dense everywhere in *physical* space $E^{\|}$. Therefore only a subset of the point lattice is chosen, which consists of lattice sites in the *acceptance window* defined in the *orthogonal* space $E^{\perp}$; particle properties are ascribed to these lattice sites. Lattice sites outside correspond to phasonic degrees of freedom (see section 3.1). In the case of the *canonical* cut-and-project method the acceptance window corresponds to a projection of the Wigner-Seitz cell. This is a primitive cell with a clear construction rule. Details for the implementation are given in section 7.

2.4 Periodic approximant

Phasonic distortion results by defining the acceptance window by a distorted basis[11]. For the cut-and-project method used here, the subset is projected into the basis of the perfect quasicrystal to get equal length scales.

If the physical space $E^{\|}$ is chosen totally irrational, the orbit is nonperiodic[9] and the physical space intersects exactly one lattice point, in the following, the origin. If $E^{\|}$ is rational, lattice points are intersected at equal intervals. The cut-and-project method then delivers periodic structures. If the hyperangles are approximated, a *periodic approximant* is generated; it's a periodic crystal whose unit cell is similar to a part of the quasicrystal. Approximants with large unit cells closely resemble quasicrystals. The larger the approximant, the smaller the energy to excite long wavelength phasonic degrees of freedom and therefore the more realization possibilities there are. They have an increasingly similar composition of tiles as quasicrystals and possess similar physical properties[1]. With larger unit cells, there are better periodic approximants. According to the Hurwitz approximation theorem[12]:

$$\left| x - \frac{p}{q} \right| < \frac{1}{\sqrt{5} q^2}$$

Where x is a real number and p and q are integers. Quasicrystal growth processes could emerge along periodic approximants. In annealing processes there can also be phase transitions between approximants and quasicrystals[13].

2.5 Cut-and-project method

The *cut*-and-*project* algorithm is a method used to generate aperiodic structures in the physical space. In order to obtain quasicrystalline structures with specific length scales, a cleverly chosen subset of lattice points is *cut* out from a suitable hyperspace and *projected* onto the physical space. The hyperspace must contain the desired symmetry. To study surface quasicrystals, the physical space is $\mathbb{R}^2$. By choosing the right orientation of the physical space, symmetries can be propagated there.

In figure 1 the projection of hypercubes around the origin onto physical space is visualised. In a) an orthogonal projection of the cube-lattice leads to a regular hexagon. In b) an orthogonal projection of the 4-cube-lattice leads to a regular octagon. In b), c) and d) orthogonal projections of the 4-cube-lattice result in 5-, 8-, 10- and 12-fold rotational symmetries in minimal embedding (see section 2.1).

With the canonical cut-and-project method the one-dimensional Pell quasicrystal can be created with the angle $\phi = \frac{\pi}{8}$. This method also allows the two-dimensional Ammann-Beenker tiling to be produced with the hyperangles of the physical space $\alpha = \frac{\pi}{4}$ and $\beta = \frac{3\pi}{4}$ perpendicular to the axis of the octagonal point group 8mm (further details in section 2.5.2).

The well-known Penrose tiling and the Square-Triangle tiling can also be obtained by the cut-and-project method. A hyperrhombohedral unit cell is required in the $\mathbb{Z}^4$ minimal embedding to generate the Penrose tiling[14]. Using the $\mathbb{Z}^5$ embedding, axial Penrose tiles can be generated with the canonical choice of the acceptance window. In minimal embedding the acceptance windows can be arbitrarily complicated: In $\mathbb{Z}^4$ to generate the well-known Square-Triangle tiling, an acceptance window with 12-fold symmetry and fractal borders is required. This acceptance window can be constructed iteratively[15].

In section 3 a simulation is carried out in hyperspace. Therefore a modification of the cut-and-project method is the starting point of the hyperspace MC simulations, instead of the projection an invertible mapping is used[16]; the lattice gets mapped to the respective symmetry-adapted basis. Before the simulation, lattice sites in the acceptance window are defined *occupied*; lattice sites outside are defined *unoccupied*. So-called phasonic flips from occupied to unoccupied lattice sites can be proposed (see section 3.4); while the interaction

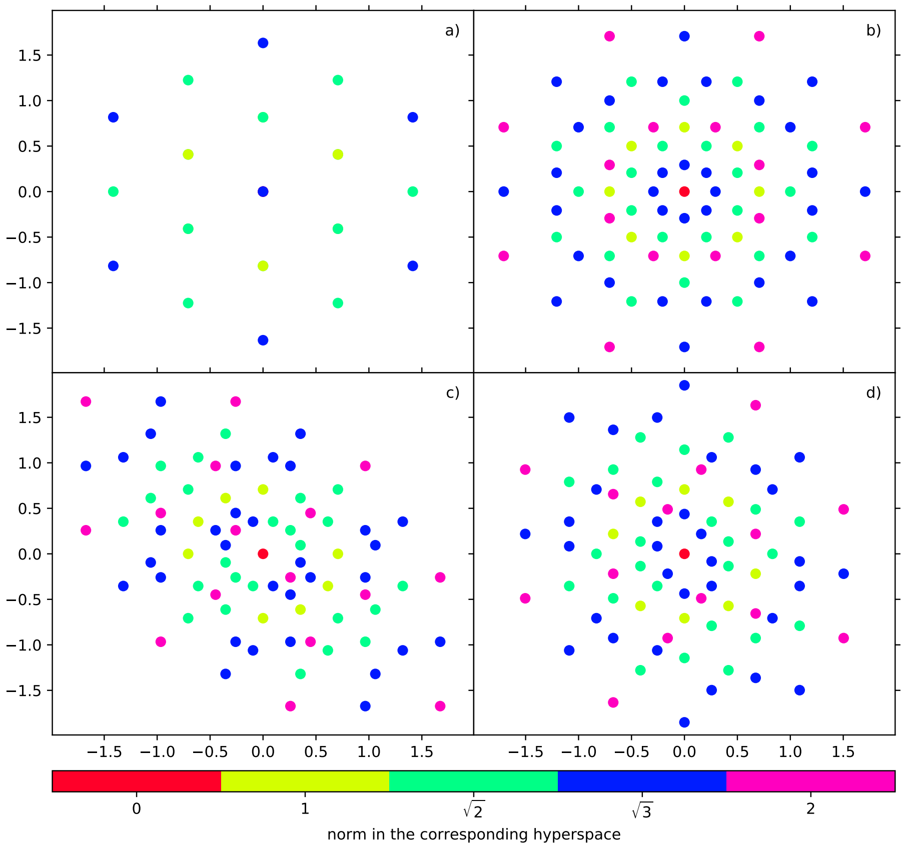

Figure 1: Visualisation of projection in the physical space of the lattice sites with entries [-1,0,1] and local symmetries: a): 6-fold rotational symmetry of the cube lattice, b): 8-fold rotational symmetry of the 4-cube lattice, c): 12-fold rotational symmetry of the 4-cube lattice, d): 5-/10-fold rotational symmetry of the 4-cube lattice. In 3D there are 27 and in 4D there are 81 possible lattice-points that are partially superimposed.

potential only works parallel to the physical space. Phasonic flips change the configuration of occupied or unoccupied lattice sites, but the hyperlattice stays unchanged. An advantage of this method is, that the distribution of phasonic flips does not have to be reconstructed, because it is given in the hyperspace coordinates at all times.

2.5.1 Silver ratio

Consider a one-dimensional physical space rotated by $\phi = \frac{\pi}{8}$ inside the two-dimensional hyperspace $\mathbb{Z}^2$. A symmetry adapted basis is given by $\hat{u}_{\|}$ and $\hat{u}_{\perp}$:

$$\hat{u}_{\|} = \begin{bmatrix} \cos(\phi) \\ \sin(\phi) \end{bmatrix} = \frac{1}{\sqrt{4-2\sqrt{2}}} \begin{bmatrix} 1 \\ \sqrt{2}-1 \end{bmatrix}$$

$$\hat{u}_{\perp} = \begin{bmatrix} -\sin(\phi) \\ \cos(\phi) \end{bmatrix} = \frac{1}{\sqrt{4-2\sqrt{2}}} \begin{bmatrix} -1 \\ \sqrt{2}-1 \end{bmatrix}$$

The canonical cut-and-project method reveals the Pell sequence $P_n := 2P_{n-1} + P_{n-2}$ with $P_0 = 0$, $P_1 = 1$ for $n \in \mathbb{N}$. In figure 2a) a Pell quasicrystal consisting of two lengths L and S is shown. The arrangement can be described by the substitution rules: $L \rightarrow LSL$, $S \rightarrow L$. The corresponding transition matrix:

$$T = \begin{bmatrix} 2 & 1 \\ 1 & 0 \end{bmatrix} \begin{bmatrix} L \\ S \end{bmatrix} := \begin{bmatrix} LLS \\ L \end{bmatrix}$$

has eigenvalues: $1 \pm \sqrt{2}$ and eigenvectors: $\begin{bmatrix} 1 \pm \sqrt{2} \\ 1 \end{bmatrix}$. Hence the numerical ratio of the number of these length scales, for an infinitely large quasicrystal, is given by $1 \pm \sqrt{2}$. With the substitution, the number of occurring lengths correspond to the Pell sequence: $P_n = A_L(n)$ and $P_{n-1} = A_S(n)$ for $n > 0$. The ratio of consecutive Pell numbers approximates the silver ratio:

$$\lim_{n\to\infty} \frac{P_{n-1}}{P_n} = \sqrt{2} - 1$$

In figure 2b) the approximant $n = 3$ with the ratio 5:2 can be seen for the silver ratio. Here a phasonic distortion is adjusted by rotating the physical space from 22.5° to 21.8° so that it intersects the following points in addition to the origin:

$$z \cdot \begin{bmatrix} 2 \\ 5 \end{bmatrix} \quad \forall\, z \in \mathbb{Z}$$

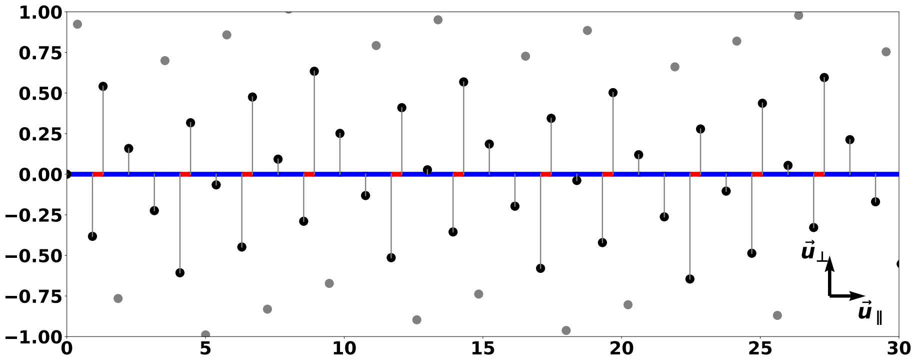

(a) Silver ratio 1:$\sqrt{2}-1$

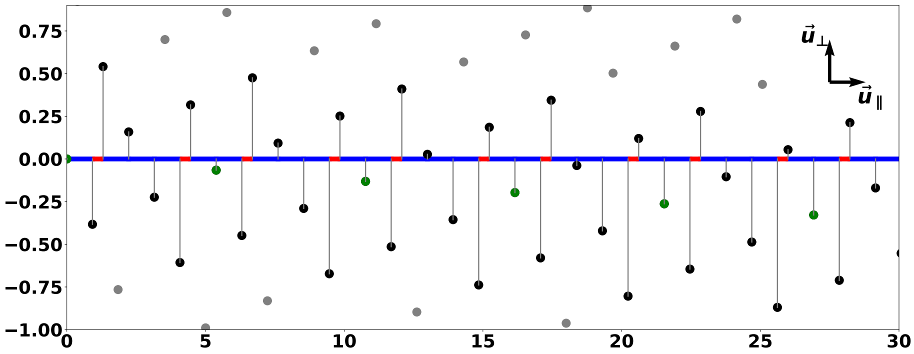

(b) Approximant 5 : 2

Figure 2: The canonical cut-and-project method in 2D to create the Pell sequence in (a) and to create a periodic approximant with sequence LSLLLSL in (b). The green dots are additional intersections with the hyperlattice. The gray dots are lattice sites outside of the acceptance window.

2.5.2 Ammann-Beenker

A matrix B where the rows form a basis and BA with $A \in GL(n, Z)$ are called generator matrices of a lattice; the action of the point group 8mm is generated by the action of eigth-fold rotation and reflection[17].

Projecting the canonical subset of $\mathbb{Z}^4$ onto the physical space with hyperspace angles $\alpha = \frac{\pi}{4}$ and $\beta = \frac{3\pi}{4}$ results in the Ammann-Beenker tiling. In section 2.2 all isometries in 4D are given. A possible generator of 8 fold symmetry in 4D is:

$$\begin{bmatrix} 0 & 0 & 1 & 0 \\ 0 & 0 & 0 & -1 \\ 0 & 1 & 0 & 0 \\ 1 & 0 & 0 & 0 \end{bmatrix}$$

A compatible basis is spanned by $\hat{x}_\parallel$, $\hat{y}_\parallel$, $\hat{x}_\perp$, $\hat{y}_\perp$; by this choice the quasicrystal is also rotational symmetric for a distorted acceptance window:

$$\hat{x}_\parallel = \begin{bmatrix} \sqrt{2}/2 \\ 1/2 \\ 0 \\ -1/2 \end{bmatrix}, \ \hat{y}_\parallel = \begin{bmatrix} 0 \\ 1/2 \\ \sqrt{2}/2 \\ 1/2 \end{bmatrix}, \hat{x}_\perp = \begin{bmatrix} \sqrt{2}/2 \\ -1/2 \\ 0 \\ 1/2 \end{bmatrix}, \hat{y}_\perp = \begin{bmatrix} 0 \\ 1/2 \\ -\sqrt{2}/2 \\ 1/2 \end{bmatrix}$$

In figure 3 a section of the perfect Ammann-Beenker quasicrystal can be seen. Ammann-Beenker is related to the Pell quasicrystal via the dual multigrid method [15].

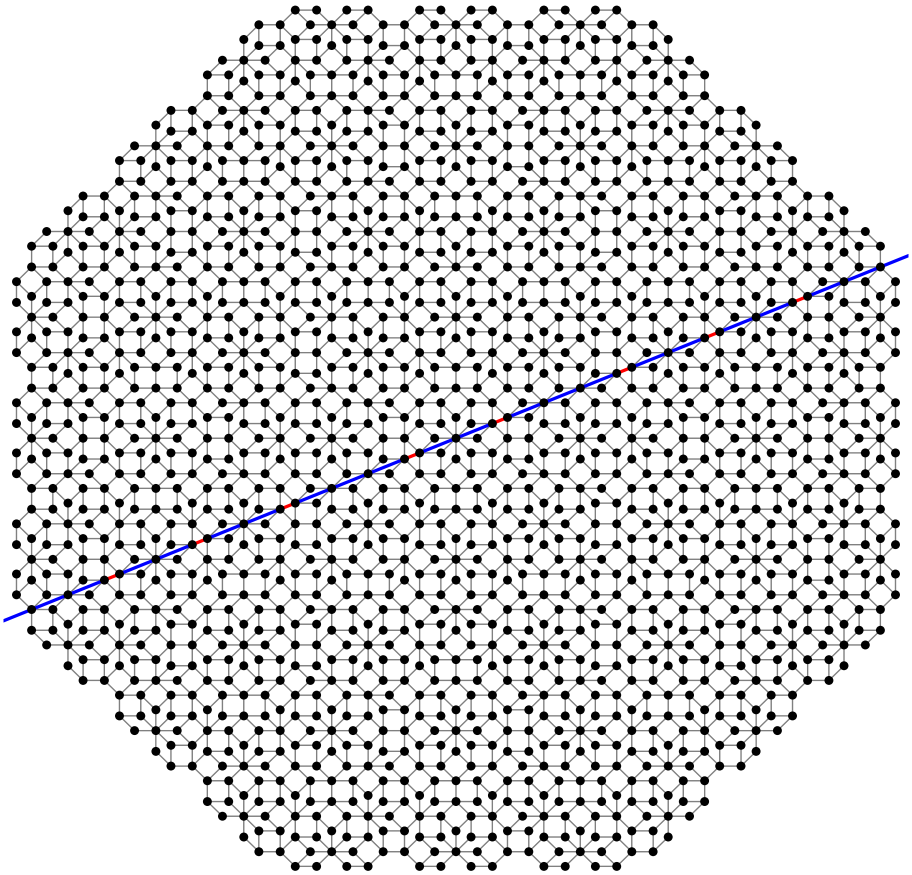

Figure 3: Ammann-Beenker tiling received with the cut-and-projection method. Inside the Pell sequence from figure 2 can be identified.

2.6 Theory of tilings

In the following, some theoretical considerations for Ammann-Beenker and Square-Triangle tiling are presented. This motivates suitable interaction potentials; the regression analysis with neural networks also depends on it.

The **Ammann-Beenker tiling** parquets the plane with an eight-fold rotational symmetry. It consists of an arrangement of squares and of rhombuses (with an angle $\pi/2$), that obeys following substitution matrix:

$$\begin{pmatrix} N_r' \\ N_s' \end{pmatrix} = \begin{pmatrix} 3 & 2 \\ 4 & 3 \end{pmatrix} \begin{pmatrix} N_r \\ N_s \end{pmatrix}$$

N_r stands for the number of rhombuses and N_s for the number of squares. For an infinite tiling the ratio of rhombuses to squares is therefore given by $\sqrt{2}$. Without overlaps, each vertex can have a circle with a radius $r = \sin \pi/8$. For these dense packed circles, each rhombus is covered by the ratio: $R_r = \sqrt{2}\pi \cdot r^2$ and each square is covered by a full circle: $R_s = \pi \cdot r^2$.
The packing density for the close packed Ammann-Beenker quasicrystal is given by:

$$\frac{R_r \cdot \sqrt{2} + R_s \cdot 1}{\sqrt{2} + 1} \approx 0.57$$

The Ammann-Beenker quasicrystal has the smallest possible length scales $2r$ and 1. The interaction potential must be carefully chosen so that the quasicrystal prevails. The quasicrystal could compete with the square phase with length $\frac{1}{\sqrt{2}}$ or $\sqrt{2}$.

The length scale 1 occurs $\left(2 + \sqrt{2}\right) \approx 3.41$ times more often than $2r$. Therefore, it can be reasonable to model the lengths in the interaction potential individually; such that the quasicrystal has lower energy than a square phase.

The **Square-Triangle tiling** parquets the plane with a 12-fold symmetry. It consists of an arrangement of squares and equilateral triangles, that obeys following substitution matrix:

$$\begin{pmatrix} N_t' \\ N_s' \end{pmatrix} = \begin{pmatrix} 3 & 7 \\ 7 & 16 \end{pmatrix} \begin{pmatrix} N_t \\ N_s \end{pmatrix}$$

N_t is equal to the number of triangles. N_s is equal to the number of squares. The ratio of triangles to squares is therefore given by $\frac{4}{\sqrt{3}}$. Each triangle is covered by dense packed circles of radius $r = 0.5$ by the ratio: $R_t = \frac{\pi}{2\sqrt{3}}$. Each square is covered by a full circle: $R_s = \frac{\pi}{4}$.
The packing density for the closed packed Square-Triangle quasicrystal is given by:

$$\frac{R_t \cdot \frac{4}{\sqrt{3}} + R_s \cdot 1}{\frac{4}{\sqrt{3}} + 1} \approx 0.87$$

For comparison the *densest packing* of equal circles is given by: $\frac{\pi\sqrt{3}}{6} \approx 0.91$. For the square lattice circle packing it's given by: $\frac{\pi}{4} \approx 0.79$.

3 Monte Carlo simulation of phasonic flips

3.1 Hydrodynamic theory for quasicrystals

Quasicrystals have $\varphi(m)$ degrees of freedom (see section 2.1). These exist as phononic and phasonic modes or quasiparticles:

Phononic modes correspond to elementary lattice vibrations; they describe the collective translation at specific frequencies of lattice sites in physical space. Phonons play a role in determining properties such as the conductivity of heat and electricity. The dimension n of the structure corresponds to the number of phononic degrees of freedom available in the system.

Phasonic modes are collective excitations of the orthogonal space. In the physical space they correspond to a rearrangement of the tiling. All possible configurations that can be reached by single phasonic flips are described below as *general* random tiling regime. In contrast to the random tiling regime, the number of tiles may change by defects, open boundary conditions or by periodic boundary conditions with the special MC method introduced in section 3.3. Phasons play a role in elastic and dynamic properties of quasicrystals[18]. There are $\varphi(m) - n$ phasonic degrees of freedom in the system.

Phonons relax quickly (in picosecond timescales). Phasonic strains are diffusive and slow; they relax on timescales between 0.1 and 100s[18]. To study the behavior of quasicrystals over large timescales, a phasonic MC simulation is proposed in section 3.4. The simulation method neglects phononic excitations and focuses on finding stable or metastable states over long timescales.

In a phasonic MC simulation, phasonic flips to neighboring lattice sites in hyperspace are proposed. Particles tend to move to energetically favorable positions. In contrast to the example of a continuous phase field model, particles are clearly given on lattice sites in hyperspace. Because of the wave-particle duality it is conceivable that a particle can tunnel through a potential barrier. It can be measured at another energetically favorable position according to the tunneling probability.

However, this obvious explanation for phasonic flips is not suitable for some quasicrystals, e.g. consisting of colloids; since the tunneling probability depends on the mass and the potential difference of neighboring particles. The flips do not happen instantaneously, but the occurrence is beyond theory. For a large number of flips this unphysical assumption can be neglected. Individual simulation steps of the MC simulation may be improbable and do not reflect the time course of a real quasicrystal. But by favoring configurations with a low energy, the MC simulation can find for a high number of MC steps, stable and metastable states.

3.2 Quasicrystalline defects

Similar defects occur in quasicrystals as in periodic crystals. The cut-and-project method used can produce defect-free starting configurations. However, it is possible to incorporate quasicrystalline defects in hyperspace[19]. Certain defects may appear during the simulation, influenced by the potential and temperature.

Topological defects in quasicrystals can lead to a long-range phasonic strain field, where multiple phasonic flips can build up a phasonic distortion. Phasonic degrees of freedom impact the distribution of stress or can substitute crystalline defects[20].

A *phasonic defect* is a non-topological defect and is here defined to be particles outside of the acceptance window; for a selected interaction potential the corresponding phasonic flips cause often a higher energy. Like phonons, phasons are hydrodynamic modes and therefore do not cost free energy in the limit of long wavelength[2]. In order to localize these phasonic defects, a neural network can be used as described in section 5.2.

3.3 Boundary conditions

Gold or platinum have a lattice constant of about 4Å. In experiments it is possible to stabilize a quasicrystal on a smooth crystal substrate[4]. Considering a surface of size $1cm^2$, there are about 10^{16} atoms in this area. In the simulation used, particle numbers of the order 10^4 are simulated. It therefore makes sense to think about the boundary conditions.

Periodic boundary conditions can be used to minimize boundary effects by using periodic approximants. In figure 4 a simulation for the periodic approximant with the length $\frac{17}{\sqrt{2}} + 12$ with few phasonic MC steps is shown. It is noticeable that the number of individual tiles does not change as a result of the steps of the random tiling regime. In order for them to change, collective phasonic flips towards a new approximant can be proposed, while the new physical space must be scaled accordingly. This can be done with a second type of canonical MC step: First, an adjacent lattice site of a point of contact with physical space is randomly selected. Than the occupied lattice sites must be shifted into the acceptance window of this new periodic approximant. Now it's possible that the number of different tiles changes depending on the chosen potentials, while the number of particles stays constant. More on that in the outlook.

In section 4 for the research on the influence of an external potential, *open* boundary conditions are used because they are implemented speed-optimized. The advantage is that a section of the perfect quasicrystal with its phasonic degrees of freedom can be simulated directly. The number of different tiles in the random tiling regime can also change as a result of phasonic MC steps.

3.4 Theory of Metropolis Monte Carlo simulation

The *Metropolis Monte Carlo (MC)* simulation is used to calculate expected values. In the following, systems in the canonical ensemble are considered, with constant particle number N, volume V and temperature T. An MC step corresponds to the sampling of N possible new configurations. The occurrence of a configuration is proportional to the Boltzmann factor: $\propto \exp -\beta E$ with $\beta = \frac{1}{k_b T}$ and k_b the Boltzmann constant. The algorithm is chosen to be time-invariant in

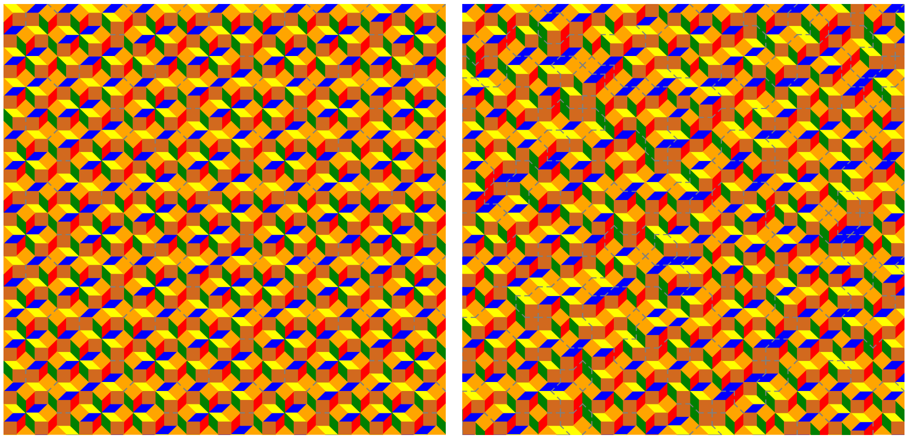

(a) Ammann-Beenker tiling (b) Random tiling configuration

Figure 4: Illustration of the phasonic MC simulation of the periodic approximant with the length $\frac{17}{\sqrt{2}} + 12$ in the tiling representation (seen in (a)). After 200 MC steps at a temperature of 0.01 with no external potential (seen in (b)). The number of individual tiles is retained in this random tiling regime. For examining anisotropies in periodic boundary conditions a simulation method is proposed in section 3.3 for which the number of tiles can change.

equilibrium; the principle *detailed balance* applies. In the MC simulation used, new configurations are suggested symmetrically; all configurations are suggested equally often. If a new configuration has a lower energy, it should always be accepted. Otherwise the acceptance probability is chosen to be proportional to the Boltzmann factor[21]:

$$p^{acc}_{old \to new} = \begin{cases} \exp\left(-\beta\left(E_{new} - E_{old}\right)\right) & \text{if } E_{new} > E_{old} \\ 1 & \text{if } E_{new} \leq E_{old} \end{cases}$$

There are too many configurations, especially for large systems, to review them all. The MC method scans random trajectories through phase space, to study statistical ensembles. It samples configurations with a frequency dependent on the Boltzmann factor. Configurations with small energies are therefore more important for the calculation of the expected value.

However, nothing can be said about the real dynamics on small time scales with this basic method. Details for the implementation will be described in section 7.

4 Results: phasonic MC simulations on a periodic substrate

The influence of an external potential on the phasonic distortion is to be investigated using the hyperspace MC simulation method. In the orthogonal components superstructures are observed.

Quasicrystals can be created on periodic substrates in experiments. For example, it is possible to grow an axial quasicrystal on a platinum 111 layer. With the proposed MC simulation, this experiment can be better understood. While surface reconstructions are neglected, the substrate on which the quasicrystal develops, can be approximated by the external potential U_{ext}:

$$U_{ext}(h) \propto \left(1 + \sin\left[\frac{2\pi}{\lambda}\left(x - \frac{y}{h}\right)\right]\right)\left(1 + \sin\left[\frac{2\pi}{\lambda}\left(x + \frac{y}{h}\right)\right]\right)$$

It corresponds to a square substrate for $h \to \infty$ and a triangular substrate for $h = \frac{\sqrt{3}}{2}$. The interaction potential of the quasicrystalline layer is approximated, in the following, by the Lennard-Jones-Gauss potential U_{LJG}, introduced by Engel *et al.*[22]:

$$U_{LJG}(r) = \frac{r_0}{r}^{12} - 2\frac{r_0}{r}^{6} - a \exp\left(-\frac{(r - r_G)^2}{2r_0\sigma^2}\right) - U_{LJG}(r_c)$$

With $r_0 = \sqrt{1 - \frac{1}{\sqrt{2}}}$, $r_G = \frac{1}{\sqrt{2}}$, $a = 0.66$, $\sigma = 0.02$ and $r_c = 2$ it is possible to stabilize the random tiling regime. Theoretically, the interaction potential is chosen so that it approximates the negative radial pair correlation function of the Ammann-Beenker tiling. With the help of simulations, it turned out that these parameters suffice at small enough temperatures T. With unsuitable parameters the quasicrystalline configuration is not very stable or the general random tiling regime can break up at different locations. A low number of vacancy defects is tolerated.

Other parameters in the simulation are the number of MC steps and the defined phasonic flips. Due to high complexity, open boundary conditions are used for around 9000 particles in the following results. The starting configurations are chosen similarly to the canonical cut-and-project method.

4.1 Quantities for the simulated quasicrystal

Quantities used to characterize the results will now be presented. They are defined in the general random tiling regime.

4.1.1 Quasicrystalline order parameter Ψ

In the general random tiling regime a phase transition between a periodic crystal and the quasicrystal will be defined by a quasicrystalline order parameter Ψ:

$$\Psi := 1 - \frac{N_1 - N_1(0)}{N_t} = \begin{cases} 1 & \text{for perfect quasicrystal} \\ 0 & \text{for perfect periodic crystal} \end{cases}$$

Where N_1 is the number of particles with neighbors at distance $S = \frac{1}{\sqrt{2}}$ with angle π. $N_1(0)$ is this number for a perfect quasicrystal and N_t is the total number of particles.

4.1.2 Analysis of number of tiles

- A pseudo order parameter similar to Ψ exists in the general random tiling regime as the ratio of rhombus tiles to square tiles:

  $$\rho := \frac{N_r}{N_s} = \begin{cases} \sqrt{2} & \text{for perfect quasicrystal} \\ 0 & \text{for periodic crystal of basic squares} \\ \to \infty & \text{for periodic crystal of basic rhombus tiles} \end{cases}$$

  Deviations from $\rho = \sqrt{2}$ indicate possible periodic approximants. In section 4.3 this quantity is defined for one-dimension as the number ratio of the length $S = \frac{1}{\sqrt{2}}$ to the length $L = 1$ as $\frac{n_1}{n_2}$ along both axes.

- L_i consists of the number ratio of individual tiles with length S to tiles with length L along an axis $i \in \{x, y\}$. The quantity $L := L_x - L_y$ can indicate an asymmetry, which may develop from a symmetrically chosen starting configuration:

  $$L := L_x - L_y = \frac{N_r\left(\frac{\pi}{8}\right) + N_r\left(\frac{7\pi}{8}\right) - N_r\left(\frac{3\pi}{8}\right) - N_r\left(\frac{5\pi}{8}\right)}{N_s\left(\frac{\pi}{4}\right)}$$

  Where $N_r(\theta)$ is the number of rhombuses with the direction of their long side defined by θ with respect to the coordinate axis. $N_s\left(\frac{\pi}{4}\right)$ is the number of by $\frac{\pi}{4}$ rotated squares.

4.1.3 Number of accepted Monte Carlo steps

N is the number of accepted Monte Carlo steps; this quantity provides information about the quality of the simulation. However, it can also depend on the length of the phasonic strains. It is noticeable that it varies locally when using an external potential. Figure 5 shows the frequency of MC flips in physical space for different wavelengths that have a similar period of the superstructure. In figure 8 an indirect connection between Ψ and N is noticeable.

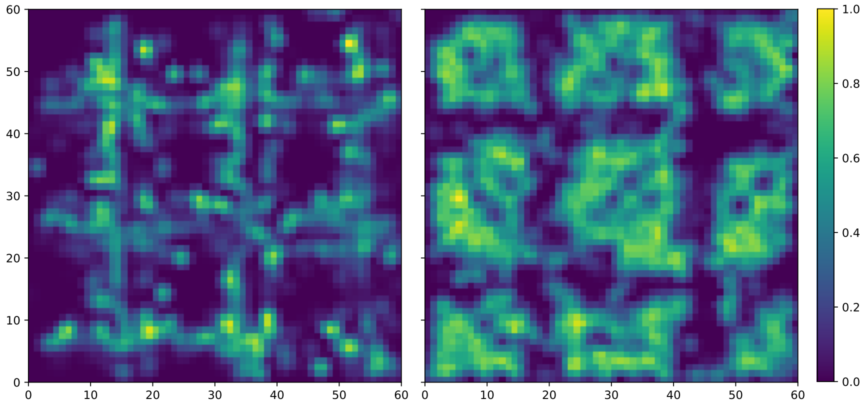

Figure 5: Normalized spatial distribution of Gaussian peaks at the location of phasonic flips for left: $\lambda = 0.1$, a bad approximant; right: $\lambda = 0.6$, a good approximant; here the quasicrystal is well preserved.

4.1.4 Fitted slope of the phasonic distortion

The fitted slope of the phasonic distortion along the coordinate axis Δa_i is defined for a direct insight into the phasonic distortion. If this quantity is averaged along all possible coordinate axes, Δa results. This quantity depends strongly on the system size and possible superstructures. The quantity $\overline{a}$ can be obtained by cutting off the edges before the fitting and considering the mean value over several simulations.

4.2 MC simulation of an initialized phasonic distortion

The hyperspace simulation simplifies the initialization and fitting of arbitrary phasonic distortions. A quasicrystal similar to Ammann-Beenker is initialized with the canonical acceptance window shifted in both orthogonal directions by the linear gradient $a_{dis}\,(\hat{e}_x + \hat{e}_y)$, depending on the distance along the axes. The change in phasonic distortion is connected to the number of different tiles. Therefore, open boundary conditions are used (see section 3.3).

The mean value of the fitted phasonic distortion Δa, averaged over 5 simulations each, is given below as $\overline{a}$. The number of MC steps is set to 10^6: a starting configuration without a phasonic distortion results in $\overline{a} = (7.17 \pm 0.04)10^{-5}$. For $a_{dis} = (8.34 \pm 0.10)10^{-3}$ without an external potential, a slight approximation to the expected angles is noticeable: $\overline{a} = (8.16 \pm 0.10)10^{-3}$. For $a_{dis} = (8.34 \pm 0.10)10^{-3}$ additional averaged over 10 different external potentials, the result is $\overline{a} = (9.1 \pm 0.9)10^{-3}$. On average, the external potential in the simulation does not simplify finding the perfect hyperspace angles of a quasicrystal or an approximant. However, the quasicrystalline structure on an external potential is mostly better preserved (see ψ in section 4.3.2).

It is remarkable that with a set phasonic distortion, steps occured in addition to overstructures. The fitted phasonic distortion Δa varies widely within the steps. Figure 6 gives examples of the phasonic distortion for a large gradient with $a_{dis} = (1.6 \pm 0.05)10^{-2}$ and a square external potential and 10^6 MC steps. For $\lambda = 1$ a step with a small gradient is noticeable: $\Delta a = (9.3 \pm 2.8)10^{-3}$. For $\lambda = 0.6$, Δa can also have negative values within a superstructure or a step.
Please note that only in this subsection the axes of the physical space are not chosen to be symmetrical for an applied phasonic distortion. This is partially the reason for the observed anisotropies in the figure 6.

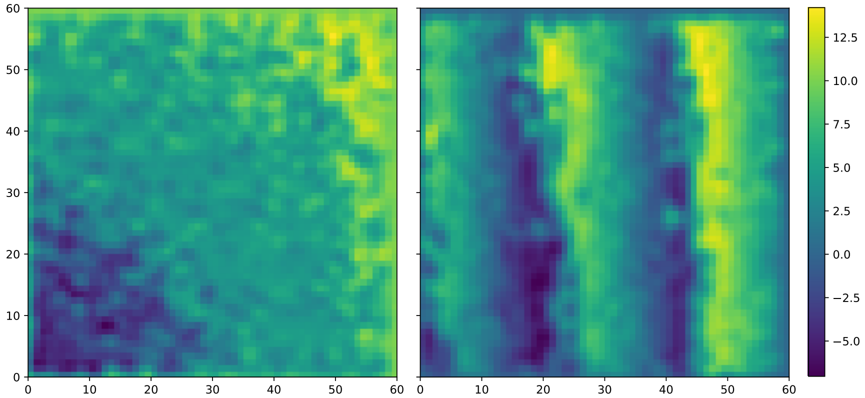

Figure 6: Spatial distribution of the phasonic distortion interpolated by Gaussian peaks at 10^6 MC steps: $a_{dis} = (1.6 \pm 0.05)10^{-2}$, left: $\lambda = 1.0$, right $\lambda = 0.6$. The colorbar shows an orthogonal component. Only in this section the basis is chosen to be asymmetrically in x_1 and x_2 direction.

4.3 Influence of an additional external potential on the quasicrystal

4.3.1 Phasonic modes

For the following analysis, the quasicrystal is chosen to be symmetric in x_1 and x_2 direction. The period of the substrate can stabilize a periodic approximant and thus the quasicrystalline order. In simulations superstructures can form in the phasonic distortion. If a multiple n of the wavelength λ corresponds to a length of the random tiling regime up to ϵ, a periodic phasonic distortion will develop at this length:

$$n\lambda = n_1 S + n_2 L + \epsilon \qquad \{n, n_1, n_2 \in \mathbb{N}\}$$

It is noticeable that the superstructure is more distinct for a small ϵ and a quasicrystalline ratio of $\frac{n_1}{n_2} \approx \sqrt{2}$. Since this equation has infinitely many solutions, only superstructures with a maximum length of ≈ 200 are allowed here. It is observed that for most triangular external potentials it is more difficult to obtain strong phasonic modes, compared to square external potentials. If an asymmetric external potential with respect to the axes of the physical space is used, specific directions along angles inside the quasicrystal have an influence on the superstructure. A coupling between possible superstructures with different angles is suspected.

As an estimate for strong superstructures, it is possible to use only the lengths of the perfect Ammann-Beenker quasicrystal for the quantities n_1 and n_2. The quasicrystalline lengths along the x-/y-axis can be calculated with the substitution rules. This results in the following transition matrix:

$$\begin{pmatrix} S' \\ L' \end{pmatrix} = \begin{pmatrix} 3 & 2 \\ 4 & 3 \end{pmatrix} \begin{pmatrix} S \\ L \end{pmatrix} .$$

Here $S = 1/\sqrt{2}$ and $L = 1$ are lengths occurring in the quasicrystal along the axes. The initial sequence of the canonical cut-and-project method is given by: SLSLSSLSLSLSSLSLSSLSLSLSSLSLSSLSLSSLSLSLSSLSLSSLSLSLSSLSLSS.

Figure 7 shows examples of how superstructures can be predicted for a triangular external potential. In figure 7A) an averaged result is shown for a simulation without an external potential. Here the occurring orthogonal modes are evenly distributed. In figure 7B) and C) for $h = \frac{\sqrt{3}}{2}$ is shown, that certain orthogonal modes can be amplified with an external potential. A triangular external potential is used here to show that an asymmetry can arise between the axes. In B) a wavelength of $\lambda = 0.05$ is used. Despite a limited simulation box, this mechanism can be illustrated for small wavelengths, since a multiple of the wavelength can correspond to many lengths in the random tiling regime. Table 1 shows theoretically calculated possible superstructures along the $i \in \{x, y\}$ direction. Here, ϵ_i indicates the difference between the quasicrystalline length and a multiple of the wavelength. In figure 7 the theoretically calculated superstructures from table 1 are shown in color. Thus, in this example, strong modes of phasonic distortion can be traced back to this theoretical calculation.

In C) another example of a triangular superstructure can be seen; for the theoretical prediction it's required to consider periodic approximants. The lengths of the notable superstructure L_i are: $L_x \approx 13.36396 = 89 \cdot \lambda \pm \epsilon$ and $L_y \approx 13.66430 = 91 \cdot \lambda \pm \epsilon$, with a small $\epsilon \approx 1.2 \cdot 10^{-5}$.

In addition to the strong superstructures discussed, the spectrum also contains other frequencies and a noise that increases at low frequencies. On the one hand, this is due to the finite simulation box, on the other hand, the spectrum can also be overlaid by other suitable superstructures in the random tiling regime.

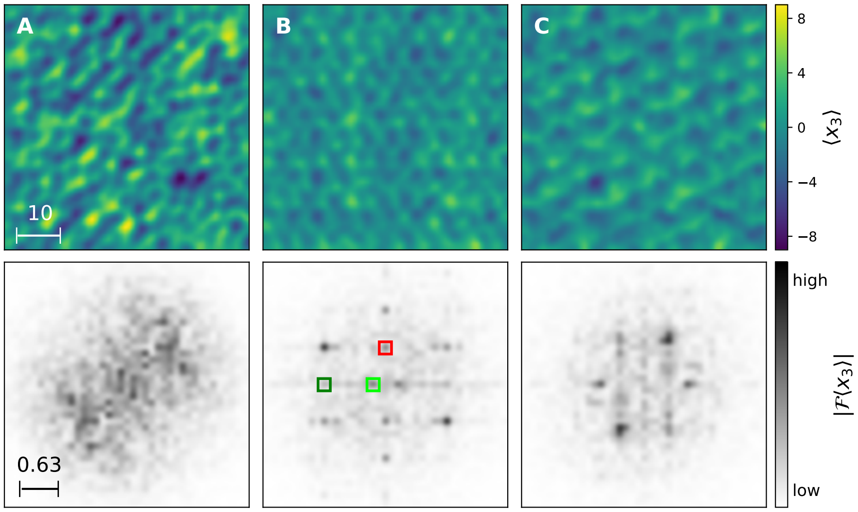

Figure 7: Prediction of the periodic superstructure in the phasonic distortion over a quasicrystal interpolated by Gaussian peaks at 10^6 MC steps. A: Without external potential, B: $\lambda = 0.05$ stretched triangular superstructure, C: $\lambda = 0.150157$ triangular superstructure. The calculated modes of figure B can be seen in table 1. Further quantities can be seen in table 2.

x-period	ϵ_x	y-period	ϵ_y
1.08	$4.87 \cdot 10^{-2}$	$6.31 \cdot 10^{-1}$	$5.05 \cdot 10^{-3}$
$6.80 \cdot 10^{-1}$	$8.72 \cdot 10^{-2}$	$3.16 \cdot 10^{-1}$	$1.01 \cdot 10^{-2}$
$5.39 \cdot 10^{-1}$	$9.74 \cdot 10^{-2}$	$2.18 \cdot 10^{-1}$	$1.52 \cdot 10^{-2}$
$4.25 \cdot 10^{-1}$	$3.45 \cdot 10^{-2}$	$2.10 \cdot 10^{-1}$	$1.52 \cdot 10^{-2}$
$3.05 \cdot 10^{-1}$	$8.32 \cdot 10^{-2}$	$1.62 \cdot 10^{-1}$	$2.02 \cdot 10^{-2}$
$2.62 \cdot 10^{-1}$	$5.27 \cdot 10^{-2}$	$1.58 \cdot 10^{-1}$	$2.02 \cdot 10^{-2}$
$2.10 \cdot 10^{-1}$	$4.04 \cdot 10^{-3}$	$1.29 \cdot 10^{-1}$	$2.53 \cdot 10^{-2}$
$1.76 \cdot 10^{-1}$	$4.46 \cdot 10^{-2}$	$1.26 \cdot 10^{-1}$	$2.53 \cdot 10^{-2}$
$1.62 \cdot 10^{-1}$	$1.82 \cdot 10^{-2}$	$1.07 \cdot 10^{-1}$	$3.03 \cdot 10^{-2}$
$1.51 \cdot 10^{-1}$	$9.33 \cdot 10^{-2}$	$1.05 \cdot 10^{-1}$	$3.03 \cdot 10^{-2}$

Table 1: Some theoretical possible periods for length of the Ammann-Beenker quasicrystal up to 200 for the simulation in figure 7-B. A small ϵ and small periods indicate a fitting superstructure, marked in colors.

	A	B	C
ρ	1.485 ± 0.025	1.445 ± 0.004	1.449 ± 0.005
L_x	1.222 ± 0.009	1.2153 ± 0.0020	1.210 ± 0.006
L_y	1.216 ± 0.013	1.2163 ± 0.0024	1.215 ± 0.005
N	$(2.26 \pm 0.09) \cdot 10^{5}$	$(1.267 \pm 0.022) \cdot 10^{5}$	$(1.291 \pm 0.018) \cdot 10^{5}$
Ψ	$(4.27 \pm 0.07) \cdot 10^{-1}$	$(7.053 \pm 0.027) \cdot 10^{-1}$	$(7.078 \pm 0.025) \cdot 10^{-1}$
Δa	$(7.17 \pm 0.04) \cdot 10^{-5}$	$(1.0259 \pm 0.0004) \cdot 10^{-4}$	$(1.4767 \pm 0.0015) \cdot 10^{-5}$

Table 2: The quantities from section 4.1 for the results of figure 7. The quantities are explained in section 4.3.2.

4.3.2 Overview: MC-Simulation with external potential

Now several simulations with 10^5 MC steps each are carried out for $\lambda \in \Lambda$:

$$\Lambda \coloneqq \{0.05n \mid n \in \mathbb{N} \wedge n \leq 30\}$$

In figure 8, an overview of the quantities from section 4.3, averaged over 5 simulations with random quasicrystalline starting configurations and over the course of each simulation in 10 equal steps, is presented. The results are plotted against λ. In order to stabilize the perfect Ammann-Beenker tiling, a much more complicated interaction potential than the Lennard-Jones-Gauss potential used is needed. For this reason, the quantities for the perfect Ammann-Beenker tiling differ from those obtained using the chosen interaction potential. The

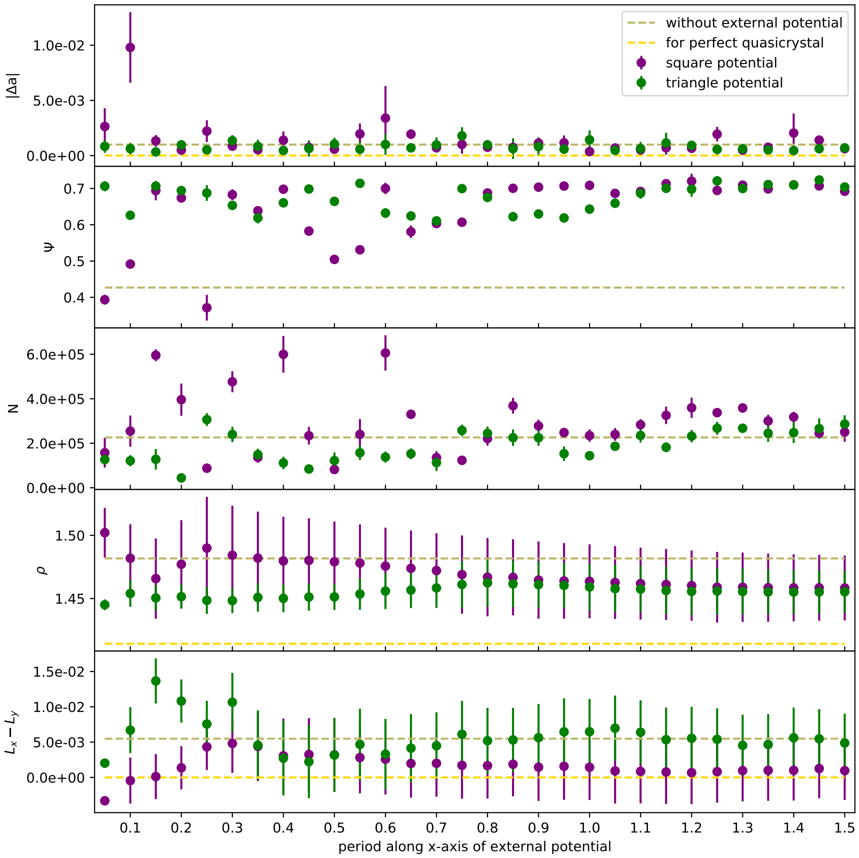

Figure 8: The averaged quantities from section 4.1 are plotted against λ with 10^5 MC steps. Errors are impacted by open boundary conditions. For a perfect quasicrystal $\Psi = 1$.

expectation that an additional external potential can better stabilize an axial quasicrystal is confirmed. Important results about figure 8 are discussed below:

It is noticeable that the order parameter Ψ for an external potential is usually closer to the quasicrystal than without an external potential. An external potential can stabilize the initialized quasicrystal. It is also noticeable that the parameter increases for longer wavelengths, while less strong modes can be observed. This could be due to the fact that possible superstructures cannot be found because of the size of the initialized quasicrystal.

A rather direct connection between the number of particles N and the order parameter Ψ is striking, especially for the square external potential. An external potential can restructure phasonic strains (see figure 6) and, by doing so, possibly change the phasonic degrees of freedom. Configurations with a higher Ψ may have a larger entropy (see outlook).

The ρ quantity differs for the triangular and the square external potential at small wavelengths. It takes on similar values for a square external potential as for a simulation conducted without an external potential; while a triangular external potential takes on values closer to a perfect quasicrystal. This difference is due to the fact that a square external potential generates mostly stronger superstructures compared to the triangular external potential; in contrast, the triangle external potential generates modes in the superstructure that are less clearly distributed. Therefore, smaller approximants are accepted more easily for the square external potential. At longer wavelengths, the quantities of the square external potential approach the quantities of the triangular external potential. In this range, the values for ρ are similar because the number of possible superstructures decreases and because of the limited simulation box used.

As motivated in section 4.3, the quantity $L_x - L_y$ takes on larger values for a triangular external potential. The initialized structure is symmetric in x and y direction. By using an asymmetric external potential anisotropy will be induced.

The results of the quantity $|\Delta a|$ may appear random at first glance, with outliers being noticeable. An attempt is made to arrange this quantity along the length of the phasonic superstructures; with the expectation that for simulations with a larger superstructure better approximants and therefore smaller fitted slopes can be found. In table 3 the averaged fitted slopes for different ϵ are compared to simulations with visually identified superstructures: For the *theoretically* calculated superstructures 100 simulations with randomly shifted initial configurations are averaged. Those superstructures correspond to the smallest possible occurring length that differs only by ϵ (as motivated in section 4.3.1); only lengths corresponding to the perfect Ammann-Beenker tiling (AB) as well as good approximants (Ap) are taken as reference. Additional errors for the theoretical calculation result from the fact that it is not taken into account which superstructures finally prevail. For the *visually* identified superstructures, 5 simulations with randomly shifted initial configurations are averaged. A possible phasonic superstructure can only be visually identified in about half of the simulations. This approach is therefore particularly error prone.

Further contributions to the errors are the possibility that superstructures may not develop due to the limited number of particles and the boundary conditions used. The results also depend on the set of used wavelengths of the substrate (see figure 8). Despite the large number of sources of error, it is still possible to significantly confirm the expected outcome for the square external potential. However, it should be noted that the results for the triangular external potential just provide a tendency, they lack statistical significance. Compared to a square external potential, the superstructures for a triangular external potential are typically less distinctive; their theoretical prediction is more complex.

	Square	Triangle
AB: $\epsilon = 0.007$	$(-8.3 \pm 0.6) \cdot 10^{-6}$	$(-0.3 \pm 1.9) \cdot 10^{-6}$
AB: $\epsilon = 0.3$	$(-6.7 \pm 0.7) \cdot 10^{-5}$	$(1 \pm 9) \cdot 10^{-6}$
Ap: $\epsilon = 0.0013$	$(-2.2 \pm 0.9) \cdot 10^{-5}$	$(-0.4 \pm 1.0) \cdot 10^{-6}$
Ap: $\epsilon = 0.007$	$(-3.9 \pm 0.9) \cdot 10^{-5}$	$(-1.0 \pm 1.2) \cdot 10^{-5}$
Visually:	$(-2.7 \pm 2.1) \cdot 10^{-5}$	$(-9.8 \pm 2.5) \cdot 10^{-5}$

Table 3: Fitted $|\Delta a|$ along the associated superstructures; with 5 units of the boundary cut off and averaged over 100 simulations each with randomly chosen initial configurations. The theoretical superstructures are calculated depending on ϵ (see section 4.3.1). They are compared to visually identified superstructures; averaged over 5 simulations with randomly chosen initial configurations. The expectation that better approximants are found more easily for larger superstructures is partially be confirmed.

5 Neural network

This section examines how well neural networks can identify quasicrystals. A quasicrystalline structure is fully described by its representation in hyperspace. Thus, neural networks are proposed that can contribute to the reconstruction of quasicrystals in hyperspace.

The neural network model used is based on the *perceptron* algorithm, which is in its basic form, a single-layer linear classifier with a binary classification. In 1958 this algorithm was introduced by Frank Rosenblatt[23]. The nodes of the network are designed to mimic the neurons in our brains. The network was initially created for image recognition and classification of sonar echoes.

Based on the spike response model of neurons, the output of a neuron is a sigmoidal activation function of an incoming weighted sum and possibly a bias; while in the following, the input values of the nodes of the first layer correspond to the brightness of individual pixels. The network uses a sigmoidal activation function, like the rectified linear unit (*relu*) or its smooth version softplus rectifier, to speed up the training process and to prevent the *vanishing gradient problem* during training, by reducing vanishingly small gradients in the learning algorithm. With supervised learning it is common for layers that are further away from the output to be harder to train, since the error signal decreases exponentially as a result of the composition of the neurons. A neural network with a continuous output is called a *regression* problem. The output layer can be adjusted for negative validation data, by using a final *linear* activation function.

By adapting the weighting functions through a learning process, the neural network can be enabled to evaluate previously unknown images. The learning progress is given by a loss function, which indicates the difference between the prediction and the desired result. To minimize the loss function, the *Adam* (derived from '**Ada**ptive **M**oment Estimation') algorithm, a stochastic gradient descent method, is used for its superior performance. The algorithm was introduced by Kingma and Ba in 2014[24]. It's stochastic, because every iteration uses only a randomly chosen subset of the training data for the training. In order to determine the descent direction and the optimal increment of the weights, the gradient of the loss function along the weight parameters of the network is calculated.

The Adam method tries to optimize the weights as effectively as possible by also approximating the second order of the gradient. For this purpose, the bias-corrected exponential moving average of the gradient $\hat{m}_t$ and of the elementwise squared gradient $\hat{v}_t$ is calculated, including past time steps. With this estimation of the first and second moment the step size of the learning rate is adjusted:

$$\Delta_t \propto \frac{\hat{m}_t}{\sqrt{\hat{v}_t} + \epsilon}$$

with a proposed default value for $\epsilon = 10^{-8}$.

The processing power can be increased by a modified model of the perceptron with several layers. For more precise associations, multilayer perceptrons with hidden layers inserted are used, where each node is connected to every node of the following layer. By using two layers with at least one neuron each, it is possible to overcome the *XOR problem*; therefore hidden layer architecture is used to give the network the opportunity to access important neural logic gates (eg. AND, OR, NAND, XOR). Neural networks are not restricted to Boolean logic, according to the *universal approximation theorem* there is always a network structure that can approximate any real-valued function with arbitrary precision.

Each neuron can be a features detector. The features to be recognized become increasingly abstract the further away they are from the input. Quasicrystaline input data include built-in symmetries. The results of the neural network often are independent of translation, rotation and scaling. Theoretically, even in a general multilayer perceptron, larger feature detectors should emerge automatically. But by building the locality and the translation invariance directly into the architecture, learning can be improved. The architecture of the *convolutional neural network* (CNN) is used for this. It consists of a convolutional layer with locally overlapping identical feature detectors and a pooling layer to reduce the dimension of the data. By adding a pooling layer, rotational and scale invariance can also develop, for a carefully chosen training data set[25].

The reconstruction of quasicrystals in hyperspace is performed in [7] by reversing the projection method. An orthogonal contribution can be approximately ascribed to a particle position. To do this, the orientation of the physical space must first be determined; given by the already introduced continuous angles α and β. Then the quasicrystal with its phasonic defects is embedded in the hyperspace. To refine the approximation, possible neural networks can be used:

For the detection of hyperangles in section 5.1 a CNN is used. For the detection of phasonic flips in section 5.2, a parallel structure with a CNN and a multilayer perceptron enables good results. Since there is a large number of hyperparameters, a brief analysis is conducted to determine the optimal network architecture.

Data with a quasicrystalline structure and possible phasonic defects, are generated with the cut-and-project method (see section 2) and the phasonic MC simulation (see section 3). For the loss function the *mean squared error* (MSE) is used.

5.1 Result: Finding the orientation of the quasicrystal in hyperspace

This section aims to predict the hyperangles α and β of a quasicrystal with rank 4. It is also used to analyze how CNN's work. The data are carefully prepared using the cut-and-project method. It should be noted that different tilings can have different densities (see section 2.6). Because there is no obvious way of converting the acceptance window for the ideal tilings into one another depending on the hyperangles, a round acceptance window with radius 1 is assumed. Rotations in the range $\alpha \in (\frac{\pi}{4}, \frac{\pi}{6})$ and $\beta \in (\frac{3\pi}{4}, \frac{5\pi}{6})$ are used to generate the data sets. This corresponds to a continuous transition between quasicrystals with an 8-fold and a 12-fold rotational symmetry. A compatible basis is spanned by $\hat{x}_{\|}$, $\hat{y}_{\|}$, $\hat{x}_{\perp}$, $\hat{y}_{\perp}$:

$$\hat{x}_{\|} = -\begin{bmatrix} \sin(2\cdot\alpha) \\ \sin(0\cdot\alpha) \\ \sin(1\cdot\alpha) \\ \sin(3\cdot\alpha) \end{bmatrix},\ \hat{y}_{\|} = \begin{bmatrix} \cos(2\cdot\alpha) \\ \cos(0\cdot\alpha) \\ \cos(1\cdot\alpha) \\ \cos(3\cdot\alpha) \end{bmatrix}, \hat{x}_{\perp} = \begin{bmatrix} \sin(1\cdot\beta) \\ \sin(3\cdot\beta) \\ \sin(2\cdot\beta) \\ \sin(0\cdot\beta) \end{bmatrix}, \hat{y}_{\perp} = \begin{bmatrix} \cos(1\cdot\beta) \\ \cos(3\cdot\beta) \\ \cos(2\cdot\beta) \\ \cos(0\cdot\beta) \end{bmatrix}$$

In this section neural networks are trained to learn the angles α and β with bitmaps of the size 512x512. A bitmap is generated by superimposing, for example, Gaussian peaks centered around the lattice sides.

How does an artificial neural network learn? Persons tasked with reconstructing hyperangles will likely search for and classify centers of symmetry. Then they will look for quasicrystalline defects and then they will make an estimate of the frequency of the length scales that occur. These properties are compared to quasicrystals with known hyperangles.

Artificial neural networks with their concentrated computing power can usually calculate short-range correlations faster and more precisely than the human brain. Depending on the hyperangles, there are specific length scales and centers of symmetry (see section 2.2). A neural network can weight certain features more heavily and thus make statements about the frequencies of particular length scales or centers of symmetry. A regression network with two output neurons is used for this; since long-range orders are not particularly important a CNN is chosen.

In figure 9 and 10 examples of the test data can be seen. For rotations around the hyperangle α there are more distinctive structures than for β. There are also areas of hyperangles in which the neural network recognizes the test data differently well. The neural network does not learn the angles continuously but it's trained on certain features.

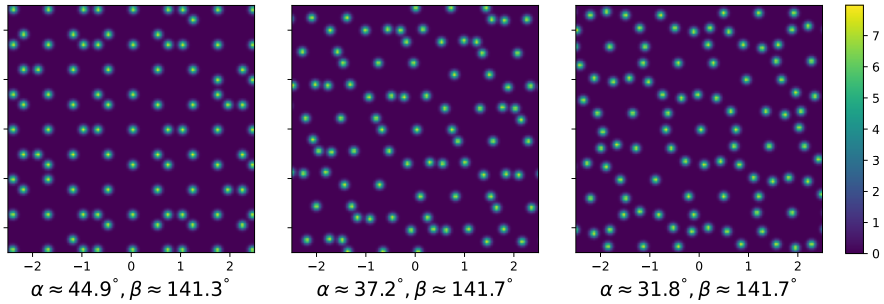

Figure 9: Example of special configurations for different hyperangles α.

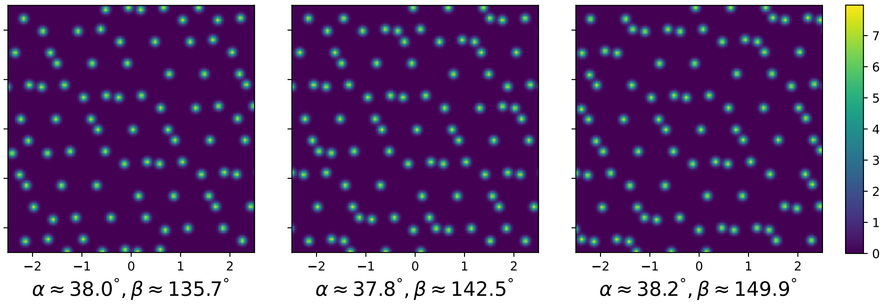

Figure 10: Example of special configurations for different hyperangles β.

To search for an efficient network structure the *differentiability* δ gets introduced. This function indicates how many correlations are available to the network, with more distant contributions being weighted more heavily:

$$\delta := \left\langle \sum_{\substack{i,j=0 \\ i>j}}^{N} \frac{|g(r_i) - g(r_j)|}{g_{max}(r_i, r_j)} \cdot \frac{(i-j)}{N} \right\rangle$$

With $g(r_i)$ is the radial distribution function, for $r_{i,j} \leq 1$, with the associated resolution N and $g_{max}(r_i, r_j)$ is a normalization factor.

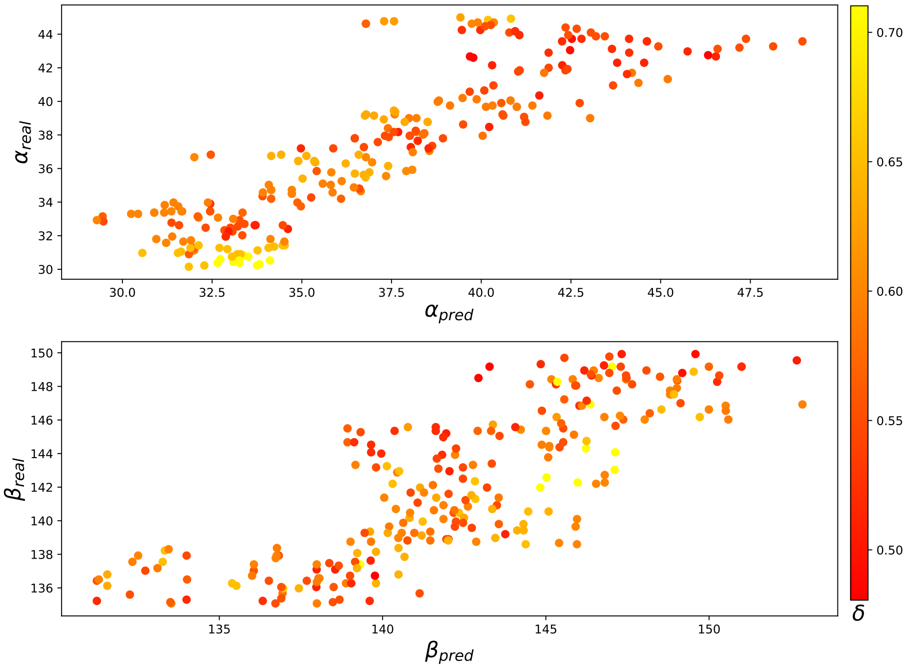

Figure 11: Test data of data set A: Predictions against reality of the hyperangles α and β of neural network A after 5 epochs. The colormap is given by δ. With increasing epochs the predictions are approaching the test data. Changes of α provide more distinctive patterns (see example in figure 9 and 10).

5.1.1 Complexity of CNN's for the learning progress

Data set A, consisting of 1000 training data and 249 test data, is generated by choosing random hyperangles in the discussed range. In figure 11 the training progress of the neural network is plotted after 5 epochs. The data set used, can contain several scales due to the chosen acceptance window. The decision criteria of a neural network are difficult to understand; therefore the results of three CNN's are compared with each other. These differ in the complexity of the network; here the number of convolutional and pooling layer (i.e. variable size of the kernel and the number of filters). The *complexity* of a neural network is the amount of neurons and weights.

The network A consists of two, B of three and C of four convolutional and max pooling layers. The test data is divided into 3 ranges according to the calculated δ, each range containing 83 test data: [high δ, medium δ, low δ].

$\langle a' \rangle$ is the averaged fitted deviation of the test input from the ideal slope. $\langle \sigma \rangle$ is here the averaged standard deviation of the difference between prediction and reality for each test input. The results are averaged over 10 full training sessions. The training data are mixed in each case. The results are also comparable to a

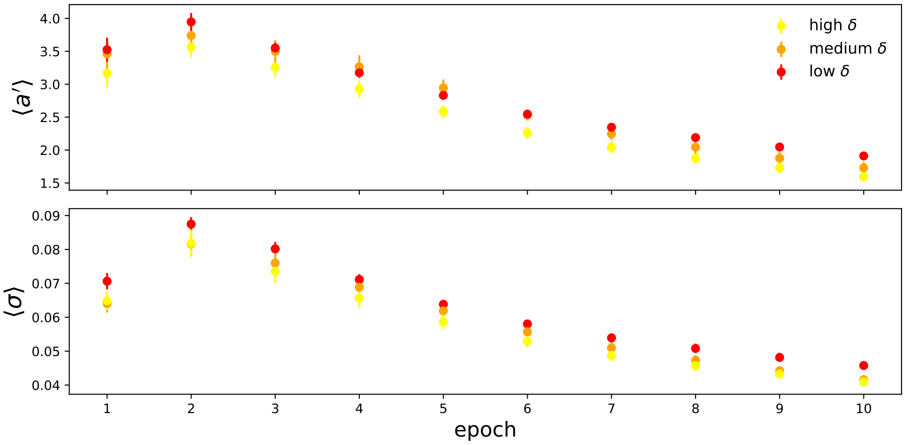

Figure 12: The data from figure 11 is divided into 3 ranges [low, medium, high] depending on the colorbar δ. For the learning process neural network A is used. ⟨a'⟩ and $\langle\sigma\rangle$ are plotted against the epochs of the learning process; they are described in section 5.1.1. The mean value over 10 full training sessions is considered here. High values of δ lead to better results, because the images have obvious lengthscales, which can be easily linked in the simple neural network through the learning process.

data set with a randomly generated initial configuration; there is no significant difference.

In figure 12 the simple network A is used. The high δ data set has a small $\langle\sigma\rangle$ and has a good fitted slope compared to the other data sets. In figure 13 the more complex network B is used. For the high δ data set ⟨a'⟩ has the best results after 10 epochs, also compared to the other neural networks. It is possible that the high δ data set is initially less prone of learning wrong features, because $\langle\sigma\rangle$ is larger. In figure 14 you can see that for the high δ data set a further increase in complexity leads to a bad validation result relative to the other data sets. This time not because of learning wrong features - $\langle\sigma\rangle$ is still large - but because it's time consuming to train such a deep network.

Therefore a kind of phase transition can be seen with increasing complexity. It is striking that the differentiability δ between length scales has an impact on the training process. One possible explanation is, that higher values of δ are clearer to the human eye, but since the neural networks used perform the operations for each neuron at a similar speed, data with a lower δ have more information. More complex neural networks have better access to this additional information. Because of the round acceptance window, different scales are available. The predictions also depend on the complexity of the neural network at which scale invariance can effectively develop.

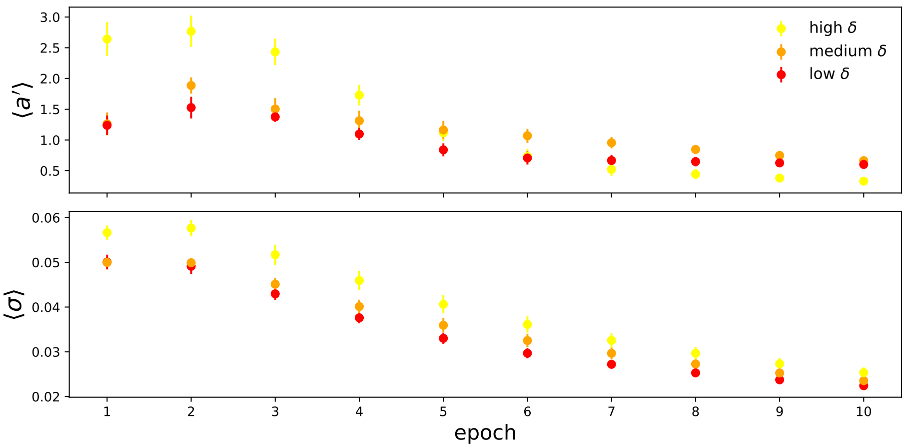

Figure 13: Continuation of figure 12: The complexity of the network has been increased in neural network B. The network is initially relatively bad at predicting the high δ data. After 7 Epochs it's quite good at it. The predictions are more evenly distributed than in figure 12 (smaller $\langle\sigma\rangle$). The neural network could therefore be less prone to learn wrong features.

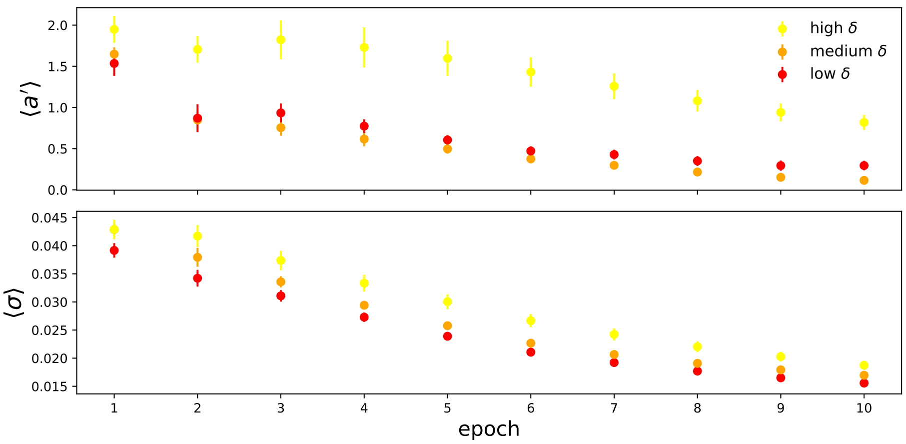

Figure 14: Continuation of figure 12 and 13: The complexity of the network has been further increased in neural network C. Now the high δ data performs worse. The network arguably has the ability to look at more complex features.

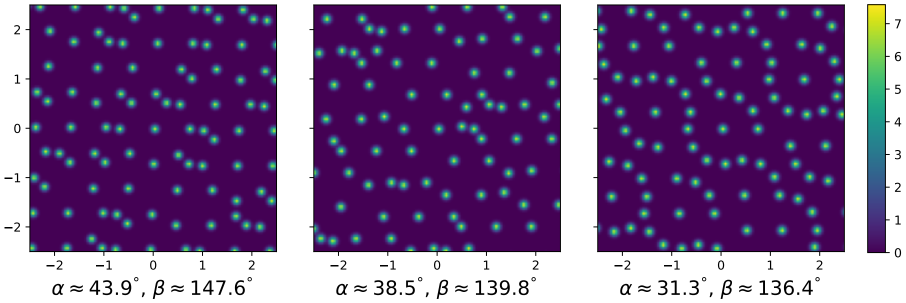

$\alpha \approx 43.9^\circ$, $\beta \approx 147.6^\circ$ $\alpha \approx 38.5^\circ$, $\beta \approx 139.8^\circ$ $\alpha \approx 31.3^\circ$, $\beta \approx 136.4^\circ$

Figure 15: Example of special configurations of the data set B.

5.1.2 More carefully prepared training/test data

Since a neural network can recognize patterns by different features, it is important to prepare the training data carefully. In order to avoid that the neural network is strongly oriented towards unspecific properties (i.e. number of particles, density, certain patterns, certain defects), data sets are used with randomly chosen translations $T = \pm 5\vec{e_i}$ in hyperspace and variances $\sigma^2 = 0.05 \pm 0.025$ of the Gaussian peaks. Rotations of the quasicrystal or different sizes of the acceptance range are neglected here. Perfect quasicrystals have a clear rotational symmetry, so it is possible to rotate the test data accordingly. The size of the acceptance window is also neglected; though the number of length scales that occur could change. Like motivated in section 5.1.1, scale invariance can develop. For real quasicrystals, no cross-scale model is usually required; the input data can be scaled accordingly. Now 1000 training data and 249 test data are generated for the data set B. In figure 15 an example of the input data of this training set is given.

If a more complex neural network D is used, the regression also works for any translations in hyperspace and variances of the Gaussian peaks. At this point it should only be mentioned, that with five convolutional and pooling layers it's possible to bring the standard deviation of the predictions to reality below 0.01. It should be noted that in order to achieve better results, more training data are probably required in this larger parameter space. In figures 16 and 17 the training progress of data set A can be compared with data set B after 100 epochs.

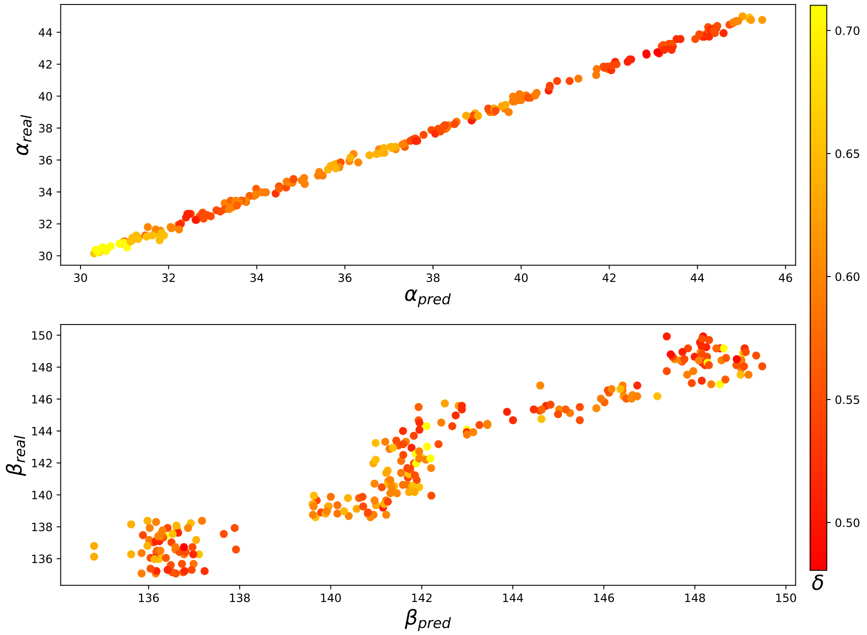

Figure 16: Predictions of data set A with neural network D after 100 epochs. The progress after 5 epochs with neural network A is shown in figure 11.

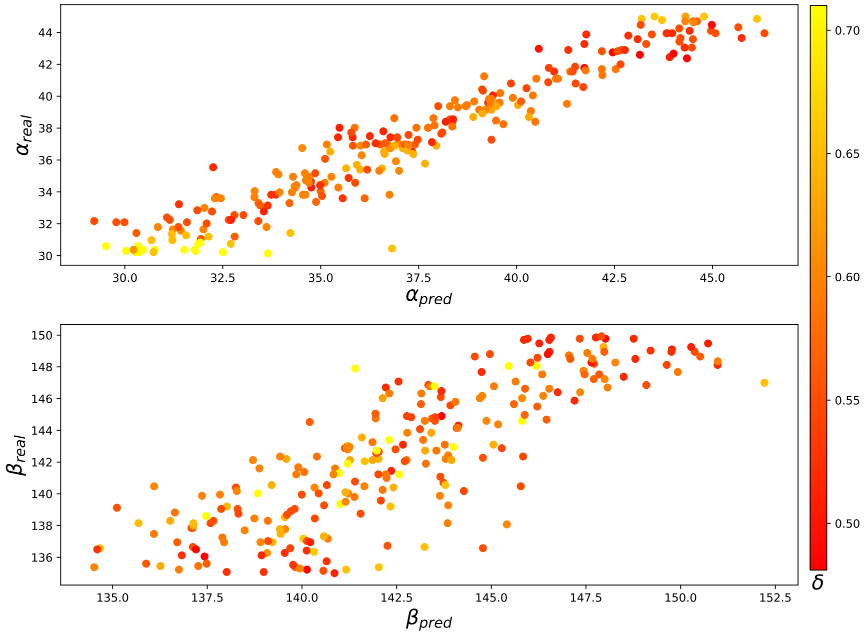

Figure 17: Predictions of data set B with neural network D after 100 epochs.

5.2 Result: Finding phasonic defects

As motivated in section 3.2, phasonic defects are here defined as rearrangements of the Ammann-Beenker tiling; the phasonic distortion depends on their distribution. Please note that the interaction potential used only approximately stabilizes the Ammann-Beenker tiling.

It will be investigated whether phasonic defects can be identified with the help of a neural network. The detection by neural networks has the advantage that only weighted sums with pre-trained weights have to be calculated. In this way, the detection of phasonic defects could be carried out easily and quickly. To motivate the model used - let's do a thought experiment:

If persons are given the task of detecting phasonic defects, they can identify them from nearby patterns. However, this procedure requires an arbitrarily complex preparation in order to be applicable for all possible phasonic flips. For configurations close to an ideal quasicrystal, detection may be easier since only certain patterns obeying the substitution rules are possible. The detection for a periodic approximant with restricted phasonic degrees of freedom is even simpler. Therefore, the model used consists partly of convolutional layers; these could recognize the short-range patterns independently of translations.

Alternatively a person can calculate the energy difference between the configurations with and without a suspected phasonic defect. To do this, the distances between neighboring particles in a certain radius are measured. The associated interaction potentials are then added up. Phasonic flips usually cause only a small change in energy; the interaction potentials of many neighboring particles again may have to be added up in order to be able to determine a difference. With a computer program and a known interaction potential, it is possible to calculate the energy analytically. A model of dense layers can learn the interaction potential from the training data; then long-range energetic contributions are added up.

In figure 18 a possible architecture of a neural network for detecting phasons is presented: A parallel structure of dense layers and a mixture of convolution and pooling layers is proposed. The influence of phasons on the energy of the system is mostly localized, since the choice of the interaction potential means that distant neighbors only make a very small contribution to the energy. With the connection of dense layering and convolutional layering, the model is converging in a reasonable time. The parallel connection can help the dense layer to train, since convolutional layers, because of their special construction, converge faster. By connecting convolutional layers in series, more and more complicated features can be extracted. During the training process, the dropout layer randomly sets certain input units to 0 with a specified rate, which serves as a regularization technique to reduce overfitting by preventing the network from relying too heavily on specific input features. In the following, with the MC simulation from section 3, data sets are generated with a number of phasonic flips built into a perfect initial configuration (i.e. Ammann-Beenker or periodic approximant). It should be noted again that the occurring phasonic flips and therefore the data sets depend on the chosen temperature and the interaction

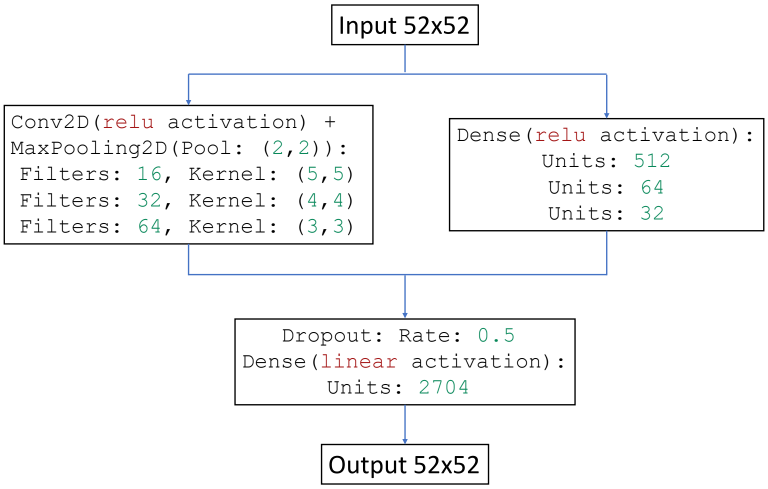

Figure 18: Neural network model used to detect phasonic defects. *Conv2D*: 2D convolutional layer to extract features. *MaxPooling2D*: dimensionality reducing layer. *Dense*: densly connected layer to previous layer. *Dropout*: layer that randomly sets certain inputs to 0 to prevent overfitting. The green numbers indicate the hyperparameters used[26].

potential. A randomly shifted section of the MC simulation with 52x52 pixels is used as input, by assigning Gaussian peaks to particle positions. The difference to the ideal tiling is used as the output.

Now the motivated model will be trained. Therefore a periodic approximant $\frac{7}{\sqrt{2}} + 5$ with periodic boundaries is chosen for generating the data set A consisting of 500 training data and 50 test data, because with periodic boundary conditions and limited phasonic degrees of freedom possible configurations can be learned easily. Later, a random tiling initial configuration based on the perfect Ammann-Beenker tiling is used to generate test data set B consisting of 50 test data, to further validate the progress of the trained network.

Validating the network with the test data of A, the loss function is at 0.51 ± 0.03. By ignoring 5 pixels at the edge, a detection rate of 83% is achieved. 8% of defects are not detected. Defects are erroneously detected with 9%. When validating phasonic deviations from the test data of B, the loss function 2.03 ± 0.03 is significantly worse. The loss function is averaged over different numbers of MC steps (10^4, 10^3, 10^2) and temperatures 0.1 and 0.05. The bad result for the reconstruction of the perfect Ammann-Beenker is not surprising. It turns out that there are significantly more possible configurations and some phasonic defects differ only by a very small energy. It therefore requires a larger bitmap and more training data for better detection; the model must also be adjusted to look more closely at long-range orders. Figure 19 shows sample test data with multiple phasonic defects and the output of the neural network.

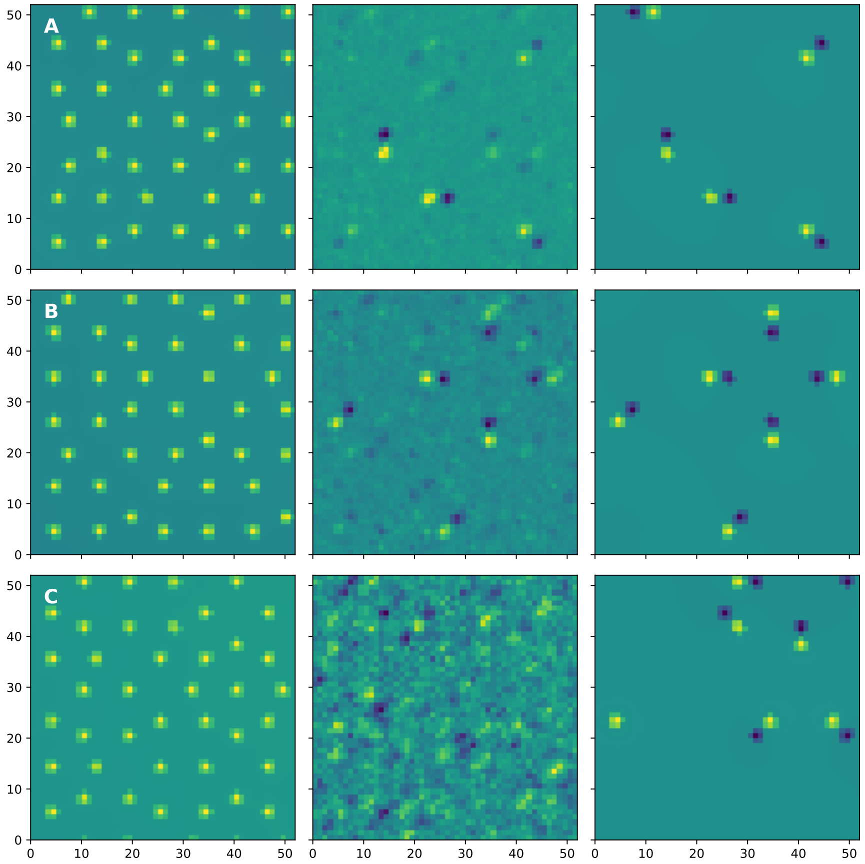

Figure 19: Left: random tiling configuration, middle: prediction of the neural network, right: actual phasonic flips. Bright dots correspond to possible defects; dark dots to ideal particle position. Detection of phasonic defects of the approximant $\frac{7}{\sqrt{2}} + 5$ with a neural network (see A and B). Obvious errors occasionally occur at the edge because the network lacks information there. For phasonic defects with a small energy, the network has problems because a larger section is required. In C an attempt is made to detect deviations from the Ammann-Beenker quasicrystal.

More detailed analysis

A section twice as large is now considered and the physical space is increased to the range [0,60]. Again a neural network is trained similar to figure 18.

For data set A, 2000 sections are chosen with random translations within physical space. For data set B, 2000 sections are chosen with random translations both within physical space and within the orthogonal space. The test data are identical for both sets of data and are independent of the training data.

In order to be able to make a quantitative statement, the number of detected defects is now given in addition to the loss function. 5 pixels are cut off at every edge, because errors often occur there. For this purpose, a color coding is introduced for following quantities, as can be seen in figure 20.

- correctly detected phasonic defects
- missing phasonic defects
- wrongly detected phasonic defects

For detection, pixels exceeding a certain threshold are used to determine the center. The prediction and the actual output are compared to analyze the type of defect.

For data set A the loss function is at 1.78 after 20 Epochs. The detection rates are: (4.37%, 30.41%, 65.22%). For data set B the loss function is at 0.65 after 20 Epochs. The detection rates are: (71.05%, 15.84%, 13.11%). An example of the validation of the test data can be seen in figure 20.

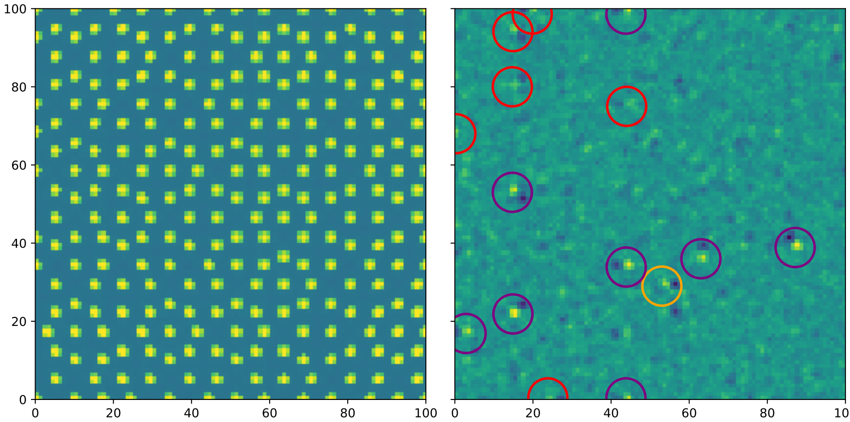

Figure 20: Left: random tiling configuration, right: prediction of the neural network trained on data set B. 5 pixels are cut off at every edge: 5 correct, 3 missing and 1 wrong.

6 Resume and outlook

In this master's thesis quasicrystals with its degrees of freedom were described by using the hyperspace concept. In section 4 the behaviour of 8-fold quasicrystals on square or triangular substrates were investigated, using phasonic MC simulations. In particular, phasonic distortion and anisotropy were studied depending on wavelengths of the substrates. In section 5, neural networks were created to identify the hyperangles of quasicrystalline structures and phasonic defects.

In future work, neural networks can be used to reconstruct quasicrystals in hyperspace. This gives an insight into the distribution of phasonic defects and gives starting configurations for phasonic MC simulations, to recreate experiments and make predictions about physical properties. Further, the phasonic MC method can be applied to explore the following topics:

- Quasicrystals have some special properties compared to periodic crystals[27]. On a periodic substrate synergies between crystalline and quasicrystalline properties can emerge.
- Studying the self-assembly of quasicrystals on a periodic substrate, by defining a grand canonical simulation method to determine if growth occurs along periodic approximants (motivated in section 2.4) or is dependent on the phasonic distortion in detail.
- Simulating multi-layer axial quasicrystals in higher-dimensional hyperspaces on substrates.
- Simulating topological defects by adapting the hyperspace[19].
- Replacing the Lennard-Jones-Gauss interaction potential by the *oscillating pair potential*[28] to improve the description of adsorption physics.
- Prediction of the influence of a periodic substrate on phasonic strains (as illustrated in figure 5), by analyzing high modes in the phasonic distortion and by calculating the entropy. The phasonic degrees of freedom can be changed by the periodic arrangement of tiles in the tiling representation.
- Improving the prediction of the superstructures in the phasonic distortion, caused by a periodic substrate (see section 4.3.1), by weighting modes depending on their period and the ϵ, by considering that different modes may influence each other and that discrete occupied lattice sites may cause a sawtooth-like orthogonal contribution.

7 Appendix

Implementation of the canonical cut-and-project method

For this method it is important to classify whether a point is inside or outside of the acceptance window, given by the convex set of the orthogonally projected unit cell. The first step is therefore to find the *convex hull* $\{H_i\}$: The cardinality of the set of edges of an n-dimensional unit cell increases by power of two. For low hyperspace-dimensions it is sufficient to implement an exhaustive algorithm, following the orientation of the surface.

To check if a hyperspace-point lies inside the acceptance window, it might be important to pay attention to the programming complexity. The *Jordan algorithm* counts the numbers of intersections with the hull of a ray, from the point of interest to infinity. The complexity scales linearly with the number of vertexes of the polygon. Because for Ammann-Beenker the acceptance window is a convex polygon and the vertex-points are sorted, it is more efficient to use a binary search to look for a triangle, with a starting point H_0 and two neighboring vertexes H_i, H_{i+1} of the convex hull that can contain the point of interest. The point is in the polygon, only if it is in the triangle. The complexity scales now logarithmically with the number of vertexes of the polygon.

Implementation of Monte Carlo method

To decide if a phasonic flip is accepted, the potential at the current position E_A and the potential at a possible destination E_B, have to be compared. The calculation of the potentials has a linear complexity. It is time-consuming to add up the potential for all points up to a certain distance. For long simulations and suitable temperatures a stable or metastable configuration can be found; then the probability of acceptance decreases. Therefore the energies rarely change and they don't have to be recalculated over and over again. The acceptance probability decreases. Only when a transition gets accepted the energies of all neighboring points need to be updated. To validate stable or metastable configurations many MC steps are simulated.

Optimizing is also done by precomputing all possible neighborhood relations; and only updating mapping functions for the indices.

Consideration of boundary condition

To minimize the occurring errors, either a larger section could be simulated, or an attempt could be made to improve the boundary conditions. A possible approach that includes periodic boundary conditions is described in section 3.3. To do this, MC steps need to change the lattice sites into the symmetry-adapted basis of a proposed approximant. Previously, hyperspace coordinates were saved with all neighborhood relations to optimize computing time.

References

[1] Wolfram Liebermeister. *Geometrie und Elektronenstruktur der Quasikristalle i-AlCuFe und i-AlPdMn.* Universität Hamburg, 1998. URL `https://www.metabolic-economics.de/pages/diploma/dipl.html`.

[2] Miriam Martinsons. *Phasonic Degrees of Freedom in Quasicrystals.* doctoralthesis, Friedrich-Alexander-Universität Erlangen-Nürnberg (FAU), 2019.

[3] Matthias Sandbrink. *Tailored Colloidal Quasicrystals.* Universitäts- und Landesbibliothek der Heinrich-Heine-Universität Düsseldorf, 2015. URL `https://books.google.de/books?id=ehwUyAEACAAJ`.

[4] Stefan Förster, Klaus Meinel, René Hammer, Martin Trautmann, and Wolf Widdra. Quasicrystalline structure formation in a classical crystalline thin-film system. *Nature*, 502:215–218, 10 2013. doi: 10.1038/nature12514.

[5] Stefan Förster. Nachwuchsgruppe / junior research group, Feb 2021. URL `http://www.forschungsschwerpunkt-nanoscience.uni-halle.de/mas/sci/sub/ngr2.oqc.html`. Last visited 2022-01-11.

[6] M. Schmiedeberg, J. Mikhael, S. Rausch, J. Roth, L. Helden, C. Bechinger, and H. Stark. Archimedean-like colloidal tilings on substrates with decagonal and tetradecagonal symmetry. *The European Physical Journal E*, 32 (1):25–34, 2010. doi: 10.1140/epje/i2010-10587-1.

[7] J Hielscher, M Martinsons, M Schmiedeberg, and S C Kapfer. Detection of phonon and phason modes in intrinsic colloidal quasicrystals by reconstructing their structure in hyperspace. *Journal of Physics: Condensed Matter*, 29(9):094002, jan 2017. doi: 10.1088/1361-648X/aa55a5. URL `https://dx.doi.org/10.1088/1361-648X/aa55a5`.

[8] John Bamberg, Grant Cairns, and Devin Kilminster. The crystallographic restriction, permutations, and Goldbach's conjecture. *The American Mathematical Monthly*, 110(3):202, 2003. doi: 10.2307/3647934.

[9] Marjorie Senechal. *Quasicrystals and Geometry.* Cambridge University Press, 2015.

[10] Steurer Walter and Sofia Deloudi. *Crystallography of quasicrystals concepts, methods and structures.* Springer Berlin, 2013.

[11] Margarita Reschke. *Zur Theorie der Approximanten in Quasikristallen.* bachelor thesis, Institut fur Theoretische und Angewandte Physik Universität Stuttgart, 2012.

[12] A. Hurwitz. Ueber die angenäherte Darstellung der Irrationalzahlen durch rationale Brüche. *Mathematische Annalen*, 39(2):279–284, 1891. doi: 10.1007/bf01206656.

[13] A. I. Goldman and R. F. Kelton. Quasicrystals and crystalline approximants, Jan 1993. URL `https://doi.org/10.1103/RevModPhys.65.213`.

[14] L Beraha, Walter Steurer, and J. Perez-Mato. The quasicrystal-to-crystal transformation. II. Landau theory. *Zeitschrift Fur Kristallographie - Z KRISTALLOGR*, 216, 11 2001. doi: 10.1524/zkri.216.11.573.22484.

[15] Christian Janot. *Quasicrystals: A Primer.* Clarendon Press, 1994.

[16] Johannes Hielscher, Miriam Martinsons, Michael Schmiedeberg, and Sebastian C. Kapfer. Phasonic Diffusion and Self-confinement of Decagonal Quasicrystals in Hyperspace. *Journal of Physics: Conference Series*, 1458(1):012018, jan 2020. doi: 10.1088/1742-6596/1458/1/012018. URL `https://dx.doi.org/10.1088/1742-6596/1458/1/012018`.

[17] Ted Janssen, Gervais Chapuis, and Marc de Boissieu. *Aperiodic Crystals: From Modulated Phases to Quasicrystals: Structure and Properties.* Oxford University Press, 06 2018. ISBN 9780198824442. doi: 10.1093/oso/9780198824442.001.0001. URL `https://doi.org/10.1093/oso/9780198824442.001.0001`.

[18] J.-B. Suck. Lattice Dynamics: Aperiodic Crystals. *Reference Module in Materials Science and Materials Engineering*, 2016. doi: 10.1016/b978-0-12-803581-8.01097-3. URL `https://www.sciencedirect.com/topics/chemistry/phason`.

[19] Jaric Marko V. *Introduction to the mathematics of quasicrystals.* Academic Press, Inc., 1989.

[20] M. Schmiedeberg, C.V. Achim, J. Hielscher, S. Kapfer, and H. Löwen. Dislocation-free growth of quasicrystals from two seeds due to additional phasonic degrees of freedom. *Phys. Rev. E*, 96:012602, 2017. URL `https://link.aps.org/doi/10.1103/PhysRevE.96.012602`.

[21] Michael Schmiedeberg. *Lecture notes Computational Physics.* Friedrich-Alexander-Universität Erlangen-Nürnberg, Winter Term 2021/22.

[22] Michael Engel and Hans-Rainer Trebin. Self-Assembly of Monatomic Complex Crystals and Quasicrystals with a Double-Well Interaction Potential. *Phys. Rev. Lett.*, 98:225505, Jun 2007. doi: 10.1103/PhysRevLett.98.225505. URL `https://link.aps.org/doi/10.1103/PhysRevLett.98.225505`.

[23] F. Rosenblatt. The perceptron: A probabilistic model for information storage and organization in the brain. *Psychological Review*, 65(6):386–408, 1958. doi: 10.1037/h0042519.

[24] Diederik P. Kingma and Jimmy Ba. Adam: A method for stochastic optimization, 2014. URL `https://arxiv.org/abs/1412.6980`.

[25] URL `https://www.deeplearningbook.org/contents/convnets.html`. Last visited 2022-01-11.

[26] Keras Team. Keras documentation: Keras layers api. URL `https://keras.io/api/layers/`. Last visited 2022-01-21.

[27] Enrique Maciá Barber. Chemical bonding and physical properties in quasicrystals and their related approximant phases: Known facts and current perspectives. *Applied Sciences*, 9(10):2132, 2019. doi: 10.3390/app9102132.

[28] Julia Dshemuchadse, Pablo F. Damasceno, Carolyn L. Phillips, Michael Engel, and Sharon C. Glotzer. Moving beyond the constraints of chemistry via crystal structure discovery with isotropic multiwell pair potentials. *Proceedings of the National Academy of Sciences*, 118(21), 2021. doi: 10.1073/pnas.2024034118.